Acoustic fluid–structure study of 2D cavity with composite curved flexible walls using graphene platelets reinforcement by higher-order finite element approach

Jeyaraj Pitchaimani, Prateek Gupta, Vasudevan Rajamohan, Olivier Polit, Ganapathi Manickam

Acoustic fluid-structure study of 2D cavity with composite curved flexible walls using graphene platelets reinforcement by higher-order finite element approach

Jeyaraj Pitchaimani[a], Prateek Gupta[b], Vasudevan Rajamohan[b], Olivier Polit[c$], Ganapathi Manickam[b]

[a]*National Institute of Technology Karnataka, Surathkal, Mangalore 575 025, India*
[b]*School of Mechanical Engineering, Vellore Institute of Technology, Vellore, 632 014, India*
[c]*LEME, UPL, Univ. Paris Nanterre, 50 rue de Sevres, 92410, Ville d'Avray, France*

Running Title: Acoustic fluid-structure interaction of 2D cavity with composite flexible walls

[$] **Corresponding author:**

E-mail: Olivier.Polit@parisnanterre.fr (Oliver Polit)

Acoustic fluid-structure study of 2D cavity with composite curved flexible walls using graphene platelets reinforcement by higher-order finite element approach

Jeyaraj Pitchaimani[a], Prateek Gupta[b], Vasudevan Rajamohan[b], Olivier Polit[c$], Ganapathi Manickam[b]

[a]*National Institute of Technology Karnataka, Surthkal, Mangalore 575 025, India*
[b]*School of Mechanical Engineering, Vellore Institute of Technology, Vellore, 632 014, India*
[c]*LEME, UPL, Univ. Paris Nanterre, 50 rue de Sevres, 92410, Ville d'Avray, France*

Abstract

In the present study, acousto-vibration analysis of 2D fluid-filled cavities/tanks having flat and curved flexible walls is made using a trigonometric function based shear deformable theory and the Helmholtz wave model for fluid domain. The governing equation formed here is solved through higher-order finite element approach. The walls are modeled by C^1 continuous 3-noded beam element and the fluid is idealized using an eight-noded quadrilateral element. Structural and coupled frequencies are evaluated for fluid-filled cavities with rigid/flexible vertical walls along with flat/curved beam on top. The sound pressure level is also predicted in the fluid domain due to a steady-state mechanical harmonic load on the top of the cavity. This investigation is conducted for metallic cavities and then extended to graphene platelets reinforced cavity. The effect of degree of fluid-structure coupling is examined assuming different fluid domains. Considering a wide range of cavity geometry and material parameters such as thickness ratio, curved beam angle, graded porosity and graphene platelets, porosity coefficient, loading of GPL, fluid medium, a comprehensive investigation is depicted to highlight their impacts on vibro-acoustic nature of fluid-filled cavities. It is observed that the dynamic characteristics of rigid and flexible wall cavities are significantly different from each other.

Keywords: Flexible walls cavity; Fluid-structure interaction; Structure and coupled frequencies*;* Sound pressure level; Air and water domains, GPLs reinforcement

[$] Corresponding author:

E-mail: Olivier.Polit@parisnanterre.fr (Oliver Polit)

1. Introduction:

In recent years, researchers have constantly focused on the development of efficient structures in absorbing the vibrational sound produced from the fluid flow over the flexible structures. Another class of fluid-structure interaction system comprising of elastic walls and an enclosed fluid cavity finds applications in construction, automobile, marine, aerospace, nuclear and several other industries. Furthermore, with the introduction of light-weight materials in these applications, the amplitude of vibration could go up due to weight reduction, and, in turn, would lead to more pressure variation and high noise level within the enclosed cavity. Several studies have been carried out considering either an open cavity with vibrating sidewalls or a closed cavity having a vibrating top wall. For an optimal design of a fluid storage cavity and fuselage, there is an increased interest among researchers to get better insights into the dynamic behavior of fluid-filled flexible cavities with curved walls through modeling and simulation. In view of this, the literature review is mainly made limiting the studies pertaining to the cavities and tanks containing fluid.

Initial studies of vibro-acoustic behavior of fluid-filled structural systems were focused on assuming tanks with flat and straight boundaries. Gladwell and Zimmermann [1] formulated a general procedure by introducing the matrix displacement approach for analyzing the acousto-structural vibration of a rectangular cavity with rigid walls having plate/ membrane on top. Later, Gladwell [2] established the governing equilibrium equations for the dynamic analysis of damped acousto-structural systems and also addressed the radiation problem using the developed formulation. Craggs [3] presented the dynamic response of a room-window system excited by the sonic boom using the plate-acoustic finite element procedure. Petyt *et al.* [4] developed an isoparametric element with 20 nodes to examine the irregular cavity shapes for the acoustic modes and experimentally validated. Wolf [5] presented the application of the modal synthesis approach to investigate the dynamic characteristics of acoustic-structural systems considering different types of vehicle's compartments. Master plan associated with the systematic theory and experiments to predict the interior acoustic characteristics of the vehicle was discussed in the work of Dowell [6]. Olson and Bathe [7] predicted the fluid-structure cavity frequencies using finite element formulation using displacement-based fluid elements whereas Sandberg and Göransson [8] introduced a symmetric finite element formulation to observe the vibro-acoustic behavior of coupled fluid-structure systems with rigid

walls by using a 2D quadratic element for the fluid domain and also a 2D interface element at the fluid-structure boundary. Later, Sandberg [9] outlined the modal based analysis for an unsymmetric fluid-structure system by extending the displacement formulation for structure and pressure/displacement potential for the fluid [8]. Alvelid [10] employed the harmonic balance method to predict the nonlinear fluid-structure interaction behavior in the fuselage of an aircraft. Scarpa and Curti [11] carried out a parametric study on coupled frequencies of a closed cavity system using the finite element method whereas Ding and Chen [12] made a symmetric finite element model to evaluate natural frequencies of a closed acoustic cavity with a top vibrating wall and compared the same with experimental results. Xiang and Huang [13] brought together a combined analytical-numerical method involving the transfer matrix approach to investigate sound radiation of a 2D fluid-structure interaction system under harmonic excitation. Harari [14] surveyed the use of finite elements to investigate the acoustic response of structures under harmonic excitations and also brought out the challenges dealing with the wave dynamics at short wavelength. Bermúdez *et al.* [15] discussed different numerical methods employed to perform elasto-acoustic analysis in time-domain and also proposed the displacement formulation to study the interface acoustic damping material. Sandberg *et al.* [16] illustrated the calculation of fluid-structure coupled frequencies of a 2-D acoustic cavity with a top vibrating wall and assuming rigid walls using typical in-house software routines. Jeong [17] carried out free vibration studies of a partially filled tank having different boundary conditions using the Rayleigh-Ritz method. Jeong and Kim [18] developed an analytical model to investigate the free vibration behavior of a fluid-filled U-shaped rectangular cavity with a flexible bottom. Hernández *et al.* [19] analyzed the vibro-acoustic control of acoustic cavity-beam interface system using finite element methodology. Hesse *et al.* [20] studied the sound radiation control of rectangular and cylindrical cavities considering the fluid-structure interaction using an analytical approach. Dinachandra and Sethuraman [21] carried out coupled fluid-structure vibration characteristics of different types of a two-dimensional fluid cavity coupled with a beam and rigid walls employing isogeometric analysis coupled with rational B-splines. Jhung and Kang [22] predicted the natural frequencies and modeshapes of partially filled rectangular fluid tanks. Bean and Yi [23] presented a mixed finite element procedure for analyzing the coupled structure-acoustic system. It may be opined here that most of the analyses associated with the fluid-filled square/rectangular tanks involved assuming rigid vertical walls and flat flexible top surface. In two-dimensional finite element analysis of the fluid-filled tanks, the top wall was modeled as a beam while the acoustic

cavity was represented using two-dimensional elements. Such study considering flexible curved walls that are of practical importance is scarce in the literature.

Recently, graphene platelets (GPLs) reinforced functionally graded porous metals (FGPM) gained a lot of attention due to their superior mechanical properties with low specific weight. Several researchers demonstrated that the properties of FGPM can be tailored through the graded distribution of both porosity and GPL. These kinds of materials with smooth property variations have the potential to replace conventional metals and fiber-reinforced composite laminate materials used in several structural applications. As the objective of the present work is to study the effect of curved elastic wall on the dynamic behavior of fluid-filled tank and cavity, for the sake of brevity, some important work on curved beams carried out recently are discussed here. Zhang *et al.* [24] studied the vibro-acoustic coupled behavior of a composite plate-cavity system using Rayleigh-Ritz method. Hosseini and Rahmani [25] used an analytical method to investigate the nonlocal effect on vibration frequencies of FG curved beams. Akbaş [26] investigated the influence of thermal load on frequencies of deep FG beams using FEM. Ganapathi and Polit [27] studied the dynamic behaviors of curved beams using an analytical method based on higher-order theory. Ebrahimi and Daman [28] analyzed the dynamic characteristics of curved FG porous beams under the influence of thermal stress using an analytical method. Ganapathi *et al.* [29] evaluated the natural frequencies of the curved beams using the finite element method based on the sine displacement model. Arefi *et al.* [30] investigated vibration frequencies of FG-GPL curved beams using an analytical method involving first-order shear deformation theory. Ganapathi *et al.* [31] examined the vibration behaviors of porous FG-GPL curved beam considering thickness stretch effect using an analytical approach. Anirudh *et al.* [32] performed a comprehensive study on porous FG-GPL curved beam using finite elements developed based on sine displacement model. Nicoletti [33] studied vibration frequencies of the curved beam using the analytical method. Recently, Chandra *et al.* [34] carried out an analytical study on vibro-acoustic phenomenon on the baffled FG plate by shear deformable theory along with Rayleigh's Integral methodology.

From the above studies, it is viewed that the available research work on the dynamic behavior of fluid-filled tanks/cavities is restricted to having an elastic flat top surface with rigid vertical walls and making use of isotropic materials, and to some limited investigation using fiber-reinforced composite materials. However, in most

practical cases, the sidewalls are also flexible and the top wall can be in the form of a curved surface. To the best authors' knowledge, there is no work available in the literature pertaining to the dynamic characteristics of fluid-filled cavity making use of FG-GPLs. This has necessitated a comprehensive study on the structural dynamics of a fluid-filled cavity with flexible sidewalls and a curved top surface made of isotropic/FGMs for the optimal design.

In this work, we analyze the effect of the flexible sidewalls and curved top wall on coupled frequencies and the vibro-acoustic response of a fluid-filled cavity made of isotropic/porous FG-GPL material. The structural model is represented by introducing a 3-noded C^1 continuity higher-order beam finite element based on trigonometric function [31, 32] and the fluid in the cavity is idealized using an eight-noded 2D isoparametric element using Helmholtz wave equations [16]. The coupled equilibrium equations resulted in unsymmetric matrix forms are transformed into symmetric ones, and the eigenvalues/eigenvectors are extracted using the standard eigenvalue approach. The sound pressure level is also predicted at a certain point in the fluid domain for a steady-state mechanical harmonic point load on the beam. The model developed here is validated, wherever possible, against the solutions available in the literature and also using commercial finite element software. A detailed investigation is performed to check the effects of graded porosity and GPL, porosity co-efficient, loading of GPL, the beam angle on coupled frequencies and acoustic response of the fluid-filled cavity.

Here, Section 2 presents the Formulation of consolidated properties; Section 3 outlines the Structural formulation and solution methodology; Section 4 deals with Beam Finite element procedure and acoustic fluid element in Section 5; validation is viewed in Section 6; Results and Discussion are highlighted in Section 7 and conclusions in Section 8.

2. Formulation of consolidated material properties

The side and top walls of the tanks shown in Fig. 1 are made of Graphene platelets (GPLs) reinforced porous metal foams. Porosity is assumed as closed-cells in graded with different patterns along the thickness and GPLs material properties are specified in terms of its geometric parameters and graded with different distribution patterns [31, 32]. Formulation of the material properties is briefly outlined here [35-39].

2.1. Distribution of porosity

The variation in material properties according to the grade distribution of porosity is specified as a function of thickness (z) as shown in Fig 2a. The density and Young's modulus are defined as [39, 40]

$$\rho(z) = \hat{\rho}[1 - e_m\lambda(z)] \;;\; E(z) = \hat{E}\left[1 - e_p\lambda(z)\right] \tag{1}$$

where $\hat{\rho}$ & $\hat{E}$ are the density and Young's modulus of the pure metal, respectively; e_m & e_p are porosity coefficients associated with density and Young's modulus respectively. $\lambda(z)$ used to define symmetric, unsymmetric and uniform distribution patterns of porosity as shown in Fig. 2a is defined as

$$\lambda(z) = \begin{cases} \cos\left(\frac{\pi z}{h}\right) & for\ symmetric\ porosity\ distriution \\ \cos\left(\frac{\pi z}{2h} + \frac{\pi}{4}\right) & for\ unsymmetric\ porosity\ distriution \\ \lambda_0 & for\ uniform\ porosity\ distriution \end{cases} \tag{2}$$

The coefficient of porosity e_p is given as

$$e_p = 1 - \bar{E}_2/\bar{E}_1 \tag{3}$$

where, $\bar{E}_1$ & $\bar{E}_2$ are the higher and lower values associated with the elastic modulus of porous GPLs beams corresponding to a particular graded pattern.

From Eq. (1), the modulus variation $E(z)/\hat{E}$ can be expressed using the density ratio ($\rho(z)/\hat{\rho}$) as [40, 41]

$$\frac{E(z)}{\hat{E}} = \left[\frac{(\rho(z)/\hat{\rho}+0.121}{1.121}\right]^{2.3} \qquad 0.15 < \rho(z)/\hat{\rho} < 1 \tag{4}$$

Substituting $E(z)/\hat{E}$ and $\rho(z)/\hat{\rho}$ from Eq. (1) into Eq. (4), a direct relationship between e_m and e_p is established as

$$e_m = \frac{1.121\left[1-\left(1-e_p\lambda(z)\right)^{\frac{1}{2.3}}\right]}{\lambda(z)} \tag{5}$$

Similarly, Poisson's ratio of the foam is defined as [41]

$$\nu(z) = 0.221e_m\lambda(z) + \hat{\nu}(0.342\,[e_m\lambda(z)]^2 - 1.21e_m\lambda(z) + 1) \tag{6}$$

Here, the overall weight of the beam is kept as same for all three different types of graded porosity. The value of λ_0 for uniform porosity case can be written as

$$\lambda_0 = \frac{1}{e_p}\left[1 - \left(\frac{\frac{1}{h}\int_{-h/2}^{h/2} \rho(z)/\hat{\rho}\, dz + 0.121}{1.121}\right)^{2.3}\right] \quad (7)$$

Based on this, equivalent elastic properties of different types of porous GPL composites are obtained. Initially, the beam is assumed to be made of FG-GPL composite material and the effective Young's modulus of the composite is obtained based on the Halpin-Tsai data model [35] whereas other properties such as $\hat{\rho}$ and $\hat{v}$ are obtained based on the rule of mixtures as follows.

$$\hat{E} = \frac{3}{8}\left(\frac{1+\alpha_{gpl}^{l}\beta_{gpl}^{l}V_{gpl}}{1-\beta_{gpl}^{l}V_{gpl}}\right)E_m + \frac{5}{8}\left(\frac{1+\alpha_{gpl}^{w}\beta_{gpl}^{w}V_{gpl}}{1-\beta_{gpl}^{l}V_{gpl}}\right)E_m \quad (8a)$$

$$\hat{\rho} = \rho_{gpl}V_{gpl} + \rho_m V_m \quad (8b)$$

$$\hat{v} = v_{gpl}V_{gpl} + v_m V_m \quad (8c)$$

where $V_m = 1 - V_{gpl}$.

V_{gpl} & V_m, represent volume fractions of graphene platelets and metal matrix respectively; material properties with subscript *'gpl'* are corresponding to graphene platelets, while subscript *'m'* represents metal matrix. Geometric parameters of the GPL ($\alpha_{gpl}^{l}, \alpha_{gpl}^{w}$) are specified as a function of thickness and aspect ratios; modulus ratios, β_{gpl}^{l}, β_{gpl}^{w} are defined as

$$\alpha_{gpl}^{l} = \frac{2l_{gpl}}{t_{gpl}}\ ;\ \alpha_{gpl}^{w} = \frac{2w_{gpl}}{t_{gpl}} \quad (9a)$$

$$\beta_{gpl}^{l} = \frac{(E_{gpl}/E_m)-1}{(E_{gpl}/E_m)-\alpha_{gpl}^{l}}\ ;\ \beta_{gpl}^{w} = \frac{(E_{gpl}/E_m)-1}{(E_{gpl}/E_m)+\alpha_{gpl}^{w}} \quad (9b)$$

2.2. GPL grading

The volume fraction of GPLs (V_{gpl}) for different graded patterns as shown in Fig. 2b is stated as

$$V_{gpl} = \begin{cases} V_1^{\,j}\left[1 - \cos\left(\frac{\pi z}{h}\right)\right] & for\ symmetric\ GPL\ distriution \\ V_2^{\,j}\left[1 - \cos\left(\frac{\pi z}{2h} + \frac{\pi}{4}\right)\right] & for\ unsymmetric\ porosity\ distriution \\ V_3^{\,j} & for\ uniform\ porosity\ distriution \end{cases} \quad (10)$$

where the superscript *j* represents the type of grading of porosity. The weight fraction of GPL (W_{gpl}) is defined as

$$V_{gpl} = \frac{W_{gpl}}{W_{gpl} + \rho_{gpl}/\rho_M(1-W_{gpl})} \quad (11)$$

The maximum value V_i in Eq. (10) is obtained based on Eqs. (10) and (11) along with the relative weights evaluated from Eq. (1) for the given porous FG-GPL case as

$$\int_{-h/2}^{h/2} V_{gpl}[1 - e_m\,\lambda(z)]\,dz = \frac{W_{gpl}}{W_{gpl}+(\rho_{gpl}/\rho_m)(1-W_{gpl})} \int_{-h/2}^{h/2} [1 - e_m\,\lambda(z)]\;dz \tag{12}$$

3. Structural formulation and solution methodology

The sidewalls of the tanks are modeled as beams and the top wall is considered as curved beam defined in terms of length L, thickness h, radius of curvature R and beam included angle θ, as depicted in Fig. 3a. Trigonometric sinusoidal shear deformation theory (SIN model) [42-44] is used to model the beam.

The displacements as a function of space and time t considered are u_1 along the length, and u_3 through beam thickness; they are defined as [42, 44]

$$\begin{cases} u_1(x,z,t) = \left(1+\frac{z}{R}\right)u_0(x,t) - z\,w'_0(x,t) + \Gamma(z)\,\gamma_0(x,t) \\ u_3(x,z,t) = w_0(x,t) \end{cases} \tag{13}$$

where γ_0 representing the shear strain in the transverse direction is given as:

$$\gamma_0(x,t) = \varphi(x,t) + w'_0(x,t) - \frac{1}{R}u_0(x,t) \tag{14}$$

The kinematics presumes three independent field variables in Eq. (13) as u_0, w_0 and φ. They are the displacements associated with axial and transverse neutral axis respectively and φ is the rotation of the cross-section. In Eq. (13) $\Gamma(z) = 0$ for Euler Bernoulli beam; $\Gamma(z) = z$ for Timoshenko beam; $\Gamma(z) = \frac{h}{\pi}\sin\frac{\pi z}{h}$ for SIN model.

Strains obtained from the kinematic equations are

$$\{\varepsilon\} = \begin{Bmatrix}\varepsilon_{xx}\\ \gamma_{xz}\end{Bmatrix} = \begin{Bmatrix} u'_0 + \frac{w_0}{R} + z\left(\frac{u'_0}{R} - w''_0\right) + \Gamma(z)\gamma'_0 \\ \Gamma'(z)\gamma_0 \end{Bmatrix} \tag{15}$$

The relationship of strains with their connected stresses can be established using constitutive law as

$$\{\sigma\} = \begin{Bmatrix}\sigma_{xx}\\ \sigma_{xz}\end{Bmatrix} = \begin{Bmatrix} C_{11}\varepsilon_{xx} \\ C_{66}\,\gamma_{xz} \end{Bmatrix} \tag{16}$$

where $C_{11} = \frac{E}{1-\nu^2}$; $C_{66} = G$

For the material model considered here, the link between shear modulus G and Young's modulus E is viewed as $E = 2G(1+\nu)$.

The generalized equations of motions for the dynamic problems can be developed in terms of displacement kinematics introducing Hamilton's principle as

$$0 = \int_0^T (\delta U_s + \delta V - \delta K)\, dt \tag{17}$$

Here, δU_s,δV & δK represent potential energy, work done by externally applied load and kinetic energy respectively, and are introduced in the variational sense and also expressed as

$$U_s(\delta_i) = \int_0^L \int_{-\frac{h}{2}}^{\frac{h}{2}} (\varepsilon^T \sigma) dz dx\,; \tag{18a}$$

$$V = -\int_0^L p\ \delta w_0\ dx \tag{18b}$$

$$K(\delta_i) = \frac{1}{2}\int_0^L \int_{-\frac{h}{2}}^{\frac{h}{2}} \rho(\dot{u}_1{}^2 + \dot{u}_3{}^2)\ dx\ dz \tag{18c}$$

where δ_i is the vector of global degrees of freedom (dof) and *p* is a transverse load applied on the surface of the beam.

Introducing Eq. (18) into Eq. (15), the weak form can be written as

$$-\int_0^L \left[\int_{-h/2}^{h/2} \delta\{\bar{u}\}^T\, \rho\{\ddot{\bar{u}}\}\ dz\right] dx + \int_0^L \int_{-h/2}^{h/2} (\delta\varepsilon_{xx}^T C_{11}\varepsilon_{xx}) dz dx + \int_0^L \int_{-h/2}^{h/2} (\delta\gamma_{xz}^T C_{66}\gamma_{xz})\, dz dx = \int_0^L [\delta\{\bar{u}\}^T\{r\}] dx \tag{19}$$

where $\{\bar{u}\}$ is the displacement vector defined as

$$\{\bar{u}\} = [F_{uw}(z)]\{\varepsilon_{uw}\} \tag{20a}$$

$$\text{Here, } [F_{uw}(z)] = \begin{bmatrix} 1 & z & \Gamma & 0 \\ 0 & 0 & 0 & 1 \end{bmatrix};\ \{\varepsilon_{uw}\}^T = \begin{bmatrix} u_0 & (\frac{u_0}{\mathrm{R}} - w_0') & \gamma_0 & w_0 \end{bmatrix};\ \{r\}^T = [0 \quad \mathrm{p}] \tag{20b}$$

Eq. (19) can be further expanded as

$$\int_0^L \delta\{\varepsilon_{uw}\}^T [-m_{uw}]\{\ddot{\varepsilon}_{uw}\}\, dx + \int_0^L \{\delta d\}^T \left[\widehat{K}_d\right]\{d\}\, \mathrm{d}x = \int_0^L \delta\{\varepsilon_{uw}\}^T \{R\} dx \tag{21}$$

$$\text{where } [m_{uw}] = \int_{-h/2}^{h/2} [F_{uw}(z)]^T \rho\, [F_{uw}(z)] dz \tag{22a}$$

$$\left[\widehat{K}_d\right] = \int_{-h/2}^{h/2} [F_\varepsilon(z)]^T C_{11} [F_\varepsilon(z)] dz + \int_{-h/2}^{h/2} \left[F_\gamma(z)\right]^T C_{66} [B_\gamma(z)] dz \quad (22b)$$

$$\{R\} = \int_{-h/2}^{h/2} [F_{uw}(z)]^T \{r\}\, dz \quad (22c)$$

$$\{F_\varepsilon\} = [1 \quad z \quad \Gamma \quad 0]; \qquad \left\{F_\gamma\right\} = [0 \quad 0 \quad 0 \quad \Gamma'] \quad (22d)$$

The vector $\{d\}^T$containing the spatial derivatives of displacement variables associated with the strains ε_{xx} and γ_{xz} is viewed as

$$\{\mathrm{d}\}^T = \left[\left(u_0' + \frac{w_0}{R}\right) \quad \left(\frac{u_0'}{\mathrm{R}} - w_0''\right) \quad \left(w_0'' + \varphi' - \frac{u_0'}{\mathrm{R}}\right) \quad \gamma_0\right] \quad (23)$$

4. **Beam Finite element (local) formulation**

4.1 Geometry approximation

The beam is divided into many elements with l_e as elemental length and the finite element procedure is carried out. Here, a 3-noded element (Fig.3b) with a local x-axis is employed. The coordinate x can be defined in terms of reduced coordinates ξ as

$$x(\xi) = \frac{1+\xi}{2} l_e \quad (24)$$

4.2 Approximations for displacements

The kinematic relation indicated in Eq. (13) is approximated in terms of displacements corresponding to the neutral axis (u_0,w_0) and rotation (φ) which are considered as primary variables. The shape functions having different orders for w_0 & φ are used to tackle the shear locking effect. Hermitian shape functions are used for w_0 and quadrative interpolation functions are used for φ as follows

$$\{w_0\} = [N_h]\left[q_{w_0}\right]; \ \{\varphi\} = \left[N_\varphi\right]\{q_\varphi\} \quad (25)$$

$$[N_h] = \left[\frac{1}{4}(\xi^3 - 3\xi + 2) \quad \frac{l_e}{8}(\xi^3 - \xi^2 - \xi + 1) \quad \frac{1}{4}(\xi^3 + 3\xi + 2) \quad \frac{l_e}{8}(\xi^3 + \xi^2 - \xi - 1)\right] \quad (26a)$$

$$\left[N_\varphi\right] = \left[\frac{\xi(\xi-1)}{2} \quad \frac{\xi(\xi+1)}{2} \quad 1 - \xi^2\right] \quad (26b)$$

Similarly, u_0 is represented by Hermite interpolation functions as $\{u_0\} = [N_h]\left[q_{u_0}\right]$. Nodal degrees of freedom at the elemental level are represented as

$$\left\{q^e_{u_0}\right\}^T = \left[u_0^{(1)}\ \ u'^{(1)}_0\ \ u_0^{(2)}\ \ u'^{(2)}_0\right]; \left\{q^e_{w_0}\right\}^T = \left[w_0^{(1)}\ \ w'^{(1)}_0\ \ w_0^{(2)}\ \ w'^{(2)}_0\right]; \left\{q^e_{\varphi}\right\}^T = \left[\varphi^{(1)}\ \ \varphi^{(2)}\ \ \varphi^{(3)}\right] \quad (26c)$$

Here the superscripts (1), (2), (3) over displacements and rotation denote the beam element node numbers (Fig. 3b). By combining the nodal vectors $\{q^e_{u_0}\}$, $\{q^e_{\varphi}\}$ & $\left\{q^e_{w_0}\right\}$, the elemental level complete nodal degrees of freedom for the element $\{q^e\}$ can be depicted as

$$\{q^e\}^T = \left[u_0^{(1)}\ \ u'^{(1)}_0\ \ w_0^{(1)}\ \ w'^{(1)}_0\ \ \varphi^{(1)}\ \ \varphi^{(3)}\ \ u_0^{(2)}\ \ u'^{(2)}_0\ w_0^{(2)}\ \ w'^{(2)}_0\ \ \varphi^{(2)}\ \right] \quad (27)$$

The vectors $\{\varepsilon_{uw}\}$ and $\{d\}$ associated with Eq. (20) and Eq. (23) are represented as

$$\{\varepsilon_{uw}\} = [B_{uw}]\{q^e\}; \qquad \{d\} = [B_{\varepsilon}]\{q^e\} \quad (28)$$

where both $[B_{uw}]$ and $[B_{\varepsilon}]$ are 4×11 matrices.

Substituting Eq. (28) into Eq. (21), the beam element matrices using the local co-ordinates level can be written as

$$[M^e]\left\{\ddot{q^e}\right\} + [K^e]\{q^e\} = \left\{f_f^e\right\} + \{f_b^e\} \quad (29)$$

Here, $[M^e]$ refers to element mass matrix in a consistent way; $[K^e]$ is typical stiffness matrix based on the linear model; the vectors $\left\{f_f^e\right\}, \{f_b^e\}$ assume the contribution from traction force and other applied loads. These matrices and vectors are given as

$$[K^e] = \int_0^l [B_{\varepsilon}]^T \left[\widehat{K}_d\right][B_{\varepsilon}]\, dx \quad (30a)$$

$$[M^e] = \int_0^l [B_{uw}]^T [m_{\varepsilon\varepsilon}][B_{uw}]\, dx \quad (30b)$$

$$\left\{f_f^e\right\} = \int_0^l [B_{uw}]^T \{R\}\, dx \quad (30c)$$

4.3 Description of Frame element

The beam element defined in Section 4.2 is aligned with the *x*-axis. For complex structures such as frames, various structural members can have arbitrary orientations, not aligned in the *x*-axis. In such cases, all the matrices and

vectors developed in the local coordinate system $\{x, z\}$ as shown in Section 4.2 must be transformed into a global coordinate system $\{X, Z\}$. The angle between the two coordinate systems is denoted as α. An approach for transforming the elemental displacement vector $\{q_e\}$ given in Eq. (27) can be developed using the transformation matrices associated with the beam coordinates and displacement vectors (local) as follows:

$$\begin{Bmatrix} \mathrm{x} \\ \mathrm{z} \end{Bmatrix} = \begin{bmatrix} cos\ \alpha & sin\ \alpha \\ -sin\ \alpha & cos\ \alpha \end{bmatrix} \begin{Bmatrix} \mathrm{X} \\ \mathrm{Z} \end{Bmatrix};\ \begin{Bmatrix} u_0 \\ w_0 \end{Bmatrix} = \begin{bmatrix} cos\ \alpha & sin\ \alpha \\ -sin\ \alpha & cos\ \alpha \end{bmatrix} \begin{Bmatrix} U_0 \\ W_0 \end{Bmatrix} \tag{31}$$

The local degrees of freedom at i^{th} node (i=1, 2, 3) given in Eq. (27) can be depicted by $\{{q_e}^{local}\}^i$ and is conveniently redefined as

$$\{{q_e}^{l}\}^i = \left\{u_0, \frac{\partial u_0}{\partial \mathrm{x}}, 0, w_0, \frac{\partial w_0}{\partial \mathrm{x}}, 0, \varphi\right\}^T \tag{32}$$

While transforming from local to global coordinate system, some additional dof appear in a global sense. The associated new dof vector at the i^{th} element node is denoted as $\{{q_e}^{g}\}^i$ which is represented as

$$\{{q_e}^{g}\}^i = \left\{u_0, \frac{\partial u_0}{\partial X}, \frac{\partial u_0}{\partial Z}, w_0, \frac{\partial w_0}{\partial X}, \frac{\partial w_0}{\partial Z}, \varphi\right\}^T \tag{33}$$

The relation between local and global displacement vectors derived using Eq. (32) can be written as

$$\{{q_e}^{l}\}^i = [T]^i \{{q_e}^{g}\}^i \tag{34}$$

Transformation matrix, $[T]^i$, is defined as :

$$[T]^i = \begin{bmatrix} c & 0 & 0 & s & 0 & 0 & 0 \\ 0 & c^2 & cs & 0 & cs & s^2 & 0 \\ 0 & -cs & s^2 & 0 & -s^2 & cs & 0 \\ -s & 0 & 0 & c & 0 & 0 & 0 \\ 0 & -cs & -s^2 & 0 & c^2 & cs & 0 \\ 0 & s^2 & -cs & 0 & -cs & c^2 & 0 \\ 0 & 0 & 0 & 0 & 0 & 0 & 1 \end{bmatrix} \tag{35}$$

Here, the variables c and s are defined as $cos\ (\alpha)$ and $sin\ (\alpha)$, respectively.

Using Eqs. (34) and (35), the element matrices associated with the frame structure in the global coordinate system is addressed as

$$[K^g]^e = [T]^T[K^l]^e[T];\ [M^g]^e = [T]^T[M^l]^e[T];\ \{f_f^g\}^e = [T]^T\{f_b^g\}^e \quad (36)$$

5. Acoustic fluid finite element formulation

5.1 Fluid domain formulation

Acoustic fluid domain equation derived based on the compressible fluid has certain assumptions like fluid is inviscid, has small translation and irrotational motion etc. Thus, the governing equilibrium equation obtained is

$$\frac{\partial^2 p}{\partial^2 t} - c_0^2 \nabla^2 p = c_0^2 \frac{\partial q_f}{\partial t} \quad (37)$$

where $\nabla^2 = \partial^2/\partial x_1^2 + \partial^2/\partial x_2^2$. Here, $p(t)$ is acoustic pressure, $q_f(t)$ is added fluid mass and c_0 is the speed of sound, respectively.

Following the finite element procedure based on weak formulation and then by introducing the pressure, $p(t)$ in terms of the generic fluid element shape function N_f and elemental nodal pressure vector p_f *i.e.* $p = N_f^T\ p_f$, the governing equation (37) at elemental level derived in terms of fluid mass and stiffness matrices, and load vectors due to traction force and added mass is presented as

$$\left[M_f^e\right]\{\ddot{p}_f\} + \left[K_f^e\right]\{p_f\} = \{f_s^e\} + \{f_q^e\} \quad (38)$$

where

$$\left[M_f^e\right] = \int_{\Omega_f} N_f^T N_f dV; \quad (39b)$$

$$\left[K_f^e\right] = c_0^2 \int_{\Omega_f} (\nabla N_f)^T \nabla N_f\ dV; \quad (39c)$$

$$\{f_s^e\} = c_0^2 \int_{\partial\Omega_f} N_f^T n_f^T \nabla p\ dS; \quad (39d)$$

$$\{f_q^e\} = c_0^2 \int_{\Omega_f} N_f^T \frac{\partial q}{\partial t} dV; \quad (39e)$$

Here, the operator $\nabla = \partial/\partial x_1 + \partial/\partial x_2$; subscripts *f* represents matrices and vectors associated with the fluid; n_f is the normal vector pointing outward from the fluid domain.

A standard 8-noded isoparametric quadrilateral fluid element as depicted in Fig. 3c with one dof per node is considered. The shape functions and their derivatives of the fluid element are:

$$N_f^T = [\, N_1\ N_2\ N_3\ \ldots\ldots\ N_8] \tag{40a}$$

where

$$N_1 = -\tfrac{1}{4}(1-\xi)(1-\eta)(1+\xi+\eta);\ N_2 = -\tfrac{1}{4}(1+\xi)(1-\eta)(1-\xi+\eta);\ N_3 = -\tfrac{1}{4}(1+\xi)(1+\eta)(1-\xi-\eta)$$

$$N_4 = -\tfrac{1}{4}(1-\xi)(1+\eta)(1+\xi-\eta); N_5 = \tfrac{1}{2}(1-\xi^2)(1-\eta); N_6 = \tfrac{1}{2}(1+\xi)(1-\eta^2); N_7 = \tfrac{1}{2}(1-\xi^2)(1+\eta)$$

$$N_8 = \tfrac{1}{2}(1-\xi)(1-\eta^2)$$

$$\nabla N = \begin{bmatrix} \frac{\partial}{\partial x} \\ \frac{\partial}{\partial y} \end{bmatrix} N_f = (\mathrm{J}^T)^{-1} \begin{bmatrix} \frac{\partial}{\partial \xi} \\ \frac{\partial}{\partial \eta} \end{bmatrix} N_f \tag{40b}$$

where J is the Jacobian matrix:

5.2 Modeling of fluid-structure coupled system

The fluid particles and elastic structure interact with each other at the boundary between the elastic and fluid domains ($\partial\Omega_{sf}$) along the normal direction to the boundary. The boundary force vector Eq. (39d) of the fluid domain f_s , expressed in terms of structural acceleration is viewed as a simplified one at the finite element level as

$$f_s = -c_0^2 \int_{\partial\Omega_{sf}} N_f^T n^T \nabla p\, dS = -\rho_0 c_0^2 \int_{\partial\Omega_{sf}} N_f^T n^T N_s\, dS\, \ddot{d}_s = -\rho_0 c_0^2 H^T \ddot{d}_s \tag{41}$$

where $H^T = \int_{\partial\Omega_{sf}} N_f^T n N_s\, dS$ is the spatial coupling matrix; *n* is the normal vector assumed as

$n = n_f = -n_s$; n_s is the normal vector pointing outward from the structure.

Similarly, the structural traction force vector f_f given in Eq. (30c) yielding coupling to the fluid medium is simplified as

$$f_f = \int_{\partial\Omega_{sf}} N_s^T n\, p\, dS = \int_{\partial\Omega_{sf}} N_s^T n\, N_f\, dS\ \ p_f = H p_f \tag{42}$$

To arrive at the system of equations for the structure-acoustic problem, the element matrices presented in Eqs. (29), (38), (41) and (42) are transformed into global frame coordinates and then assembled. The final matrix form of equations is thus depicted as

$$\begin{bmatrix} M_s & 0 \\ \rho_0 c_0^2 H^T & M_f \end{bmatrix} \begin{bmatrix} \ddot{d}_s \\ \ddot{p}_f \end{bmatrix} + \begin{bmatrix} K_s & -H \\ 0 & K_f \end{bmatrix} \begin{bmatrix} d_s \\ p_f \end{bmatrix} = \begin{bmatrix} F_b \\ F_q \end{bmatrix} \tag{43}$$

Substituting global vectors attached with structural displacement, fluid pressure, body force/point load, and added fluid mass in terms of space and time as $d_s = \overline{d_s}\ e^{i\omega t}$, $p_f = \overline{p_f}\ e^{i\omega t}$, $F_b = \overline{F_b}\ e^{i\omega t}$ and $F_q = \overline{F_q}\ e^{i\omega t}$, in Eq. (43) leads to

$$\begin{bmatrix} M_s & 0 \\ \rho_0 c_0^2 H^T & M_f \end{bmatrix} \begin{bmatrix} \overline{d_s} \\ \overline{p_f} \end{bmatrix} - \omega^2 \begin{bmatrix} K_s & -H \\ 0 & K_f \end{bmatrix} \begin{bmatrix} \overline{F_b} \\ \overline{p_f} \end{bmatrix} = \begin{bmatrix} \overline{F_b} \\ \overline{F_q} \end{bmatrix} \tag{44}$$

The coupled natural frequencies are obtained from Eq. (44) considering it as a typical eigenvalue problem neglecting the force vectors. The sound pressure response is obtained through the direct inverse of Eq. (44) for a given steady-state force/pressure induced in the fluid-filled cavity. The sound pressure level (SPL) in dB is calculated based on the definition, $20log_{10}\left(\frac{p_{rms}}{20*10^{-6}}\right) dB$, where $p_{rms} = \sqrt{p_f \bar{p}_f / 2}$ and $\bar{p}$ is the complex conjugate of the acoustic pressure p_f.

6. Validation Studies

In order to investigate the influences of curvature, graded porosity and GPLs on Sound Pressure Level (SPL) of a fluid-filled cavity with vibrating flexible walls, a finite element computer program is developed based on the description given in Section 4 and 5. This program is firstly validated against the solutions of Dinachandra and Sethuraman [21] for free vibration frequencies and SPL of a rectangular air cavity with rigid sidewalls and a straight isotropic beam on top. The dimensions and material properties of the cavity & fluid studied in Ref. [21] are L_x =10*m*; L_y = 4*m*; E=210 *GPa*; second moment of area of the beam =1.59 x 10^{-4} m^4, mass per unit length = 50 *kg/m*; density of air = 1.2 kg/m^3; sonic velocity of air = 340 *m/s*. Based on progressive mesh refinement, 30x9 is

found to be adequate to model the cavity size considered here. Structural frequencies of the beam, frequencies of the fluid cavity and coupled frequencies calculated using the present work match well with the results reported in Ref. [21] as given in Table 1. The SPL obtained at the center of the fluid cavity for a steady-state mechanical harmonic point load (1N) excited at the center of the beam is also compared with the response presented in Ref. [21] as shown in Fig. 4 to validate the response calculation.

Followed by this, natural frequencies and SPL response of the fluid cavity with isotropic flexible sidewalls and curved beam $(\theta = 30°)$ on top are calculated based on the present approach and are compared with ANSYS results as presented in Fig 5. Structural frequencies and coupled frequencies for a flexible fluid cavity-backed with curved beam $(\theta = 30°)$ are obtained using the present approach match well with the results of ANSYS as seen in Table 2. The SPL is calculated at the center of the fluid cavity for the steady-state mechanical excitation applied at the center of the curved beam and some minor deviation in the response is noticed at higher forcing frequencies. The small amount of difference between the solutions depicted in Fig.5 and Table 2 is due to the difference in the structural theories and elements used for the present analysis and in ANSYS. A typical 2-noded 3D beam element with 3 dof per node is used in ANSYS while a 3-noded higher-order 2D beam element employed for the present analysis has 8 dof at the end nodes and 2 dof in the mid-node of the beam element, see for instance in Fig. 3b.

7. Results and Discussion:

Results of a detailed numerical investigation are obtained to analyze the effect of curvature angle of the beams, nature of porosity and GPL distributions and the effect of strong- and weak-fluid coupling on natural frequency versus SPL response of a flexible rectangular fluid cavity-backed with a curved beam on top are discussed in this Section. Results associated with an isotropic beam case are also presented as it is not readily available in the literature. Porosity and GPLs are graded in symmetric, unsymmetric and uniform patterns as shown in Fig. 2 in order to analyze the effects of functional grading of porosity and GPLs on the dynamic characteristics of a fluid-filled cavity. A rectangular cavity with $L_x = 10m$ and $L_y = 4m$ is considered for the detailed investigation.

7.1 Studies on the tank with metal walls

Before performing a detailed investigation on the vibro-acoustic response characteristics of the fluid-filled tank made of porous FG-GPL material, studies are carried out for an isotropic tank with metallic sidewalls. This is done to understand the influence of side flexural walls and the curved top wall on the response characteristics of the tank. It is assumed that the flexible wall has material properties: E = 210 *GPa*, Poisson's ratio = 0.3, and density = 2500 kg/m^3. In order to analyze the influence of fluid-structure coupling effect air (ρ_0=1.21 kg/m^3; C_0= 343 *m/s*) and water (ρ_0=1000 kg/m^3; C_0= 1500 *m/s*) are considered as mediums. Free vibration frequencies of the air-filled cavity with metal sidewalls (rigid and flexible cases) with a straight beam on the top for two different *L/h* ratios (*L/h*=30,100) are given in Table 3. The effect of flexible sidewalls on both the structural and coupled frequencies is significant when compared with the rigid sidewalls case as seen in Table 3. The coupled frequency values are in general less as compared to the structural frequencies, irrespective of the sidewalls type and thickness ratio *L/h* but the difference between them is more for the rigid sidewalls case. However, while comparing the fluid frequencies against the coupled frequency values, the difference is noticeably high in general for the flexible sidewalls case and more so for the thin case. It is further observed that, for the thick case cavity with side flexible walls, more modes of natural vibration occur for a given frequency range in comparison with the rigid sidewalls case due to the vibrating nature of all the walls. This is due to the added mass effect and fluid-structure coupling effect on the natural frequencies.

The effect of curvature angle of top curved wall ($\theta=0^0,15^0\ \&\ 30^0$) on the sound pressure level of the air-filled cavity with rigid sidewalls is significant as seen in Fig. 6. From this Figure, one can observe that there is a shift in the peak amplitude associated with the fundamental frequency due to the curvature effect. There is an increase in the natural frequency because of the change in stiffness of the cavity due to the curvature effect. It is more so for *L/h = 100* case compared to *L/h=30* case. This is possibly attributed to higher enhancement of stiffness due to the curvature for the thin beam compared to the thick beam. Unlike rigid sidewalls case, the influence of curvature angles considered here on sound pressure level is not noticeably significant for the tank with flexible sidewalls as seen in Fig. 7. The shift in natural frequencies according to the curvature angle can be seen clearly in higher frequencies compared to the lower frequencies. This may be due to insignificant enhancement in overall

structural stiffness due to the increase in curvature angle for the tank with flexible sidewalls. The influence of the curvature angle of a curved beam on the sound pressure level of a water-filled tank with rigid and flexible sidewalls is shown in Fig. 8. A trend qualitatively similar to the tank with air cavity is observed for the tank with water cavity also.

7.2 Studies on fluid tank with composite material walls

The dimensions considered for the analysis of the fluid tank with metal walls are considered for this study also. For composite walls, the properties of GPLs are: E_{gpl} = 1.01 *TPa*, Poisson's ratio=0.186, Density=1062.5 kg/m^3. The length, width and thickness of GPLs are: l_{gpl} =*5nm,* w_{gpl} = *2.5nm and* t_{gpl} = *0.3nm* respectively, [30]. The effect of the porosity distribution pattern on the sound pressure level is analyzed first by considering the material without any reinforcement. The influence of three different porosity distribution pattern (c_p=*0.5*) alone on the structural and coupled frequencies of the air-filled porous tank with flexible sidewalls and straight beam on top, in absence of GPLs, is given in Table 4. Higher frequency values are obtained for the symmetric porosity distribution compared to other types of porosity distribution patterns analyzed here. The coupled frequencies are always lower than the structural frequencies as already observed from the metal tank cases. As expected, the frequency values are lower than the pure metallic case. The effect of porosity distribution patterns on the sound pressure level response for the tank with a flat top wall and curved top wall is shown in Fig. 9. A minor variation in frequencies with respect to the distribution pattern is observed in the acoustic response curves. However, it is seen that, in general, the peak amplitude associated with walls having uniform porosity distribution is relatively less. A similar study to analyze the effect of GPL distribution patterns alone on the free vibration and acoustic response characteristics of tanks having flexible sidewalls and straight beam on top is considered. The change in natural frequencies with respect to the distribution patterns of GPLs is somewhat similar to that of porosity cases. However, the frequency values are higher than the pure isotropic case, see for instance Table 3. In addition to this, it is viewed that the change in natural frequencies with respect to the distribution pattern of GPLs (W_{gpl}=*1%*) is minor and a relatively higher value is obtained for the symmetric distribution case as seen in Table 5. Due to this, there is no significant change in acoustic response except at few frequencies as seen in Fig. 10.

The effect of curvature assuming different values ($\theta = 0^0, 15^0 \& 30^0$) and wt. % of GPL ($W_{gpl}$ = 0.25% & 1%) on natural frequencies of the air and water-filled porous tank with flexible sidewalls is given in Tables 6 and 7 respectively. The sidewalls are made of composite material with symmetric porosity and symmetric GPL distribution. There is no specific trend in variation of natural frequencies with respect to curvature angle for both the wt.% of GPL assumed here. However, structural and coupled natural frequencies increase with an increase in wt.% of GPL as seen in Tables 6 and 7. The acoustic response of composite air cavities having rigid and flexible walls is examined in Figs. 11 and 12, respectively. It is seen from Fig. 11 that the increase in natural frequencies with an increase in wt.% of GPL is less and there is no noticeable shift in peak amplitudes with an increase in wt.% of GPL. The same variation in natural frequencies and sound pressure response with an increase in GPL content is observed for the flexible sidewalls case as seen in Fig.12.

The influence of curvature angle on sound pressure of air cavity with porous GPL flexible sidewalls is shown in Fig. 13 for two values of *L/h*. From Fig. 13, it is seen there is a definite shift in peaks with an increase in curvature angle for only a few modes, for example, the fourth peak in Fig. 13 (a) and the fifth peak in Fig. 13(b). There is a notable reduction in natural frequencies with an increase in curvature angle for these peaks. A similar trend in sound pressure response variation with an increase in curvature angle is observed for the air-filled cavity with rigid sidewalls as seen in Fig. 14.

The impact of curvature angle on the sound pressure of water cavity with porous GPL flexible sidewalls is shown in Fig. 15. There is no significant shift in peaks with increase in the curvature angle for the tank with a thick curved top beam as seen in Fig. 15(a). However, there is a shift in some of the peaks for the tank with a thin curved top beam as seen in Fig. 15 (b). The clear shift in peaks at some of the frequencies with an increase in curvature angle observed for the air-filled cavity is not seen in the water-filled cavity case. This indicates that the curvature angle of the top beam influences some frequencies when the density of the fluid medium is very less.

A comparison of the sound pressure level of the tanks with rigid and flexible sidewalls is shown in Fig. 16. Due to the flexible sidewalls, more modes are excited in the case of the cavity with flexible sidewalls compared to the cavity with rigid sidewalls. Similarly, the resonant amplitude of most of the modes is high for the tank with rigid sidewalls. The influence of the nature of fluid medium on the SPL response is shown in Fig. 17. The SPL of

the water-filled cavity is significantly high compared to the air-filled cavity for the *L/h = 30* case. However, there is no distinct difference in sound pressure level between the water and air-filled cavities for the *L/h = 100* case.

The influence of curvature angle on sound pressure contours of air cavity having rigid and flexible walls is shown in Fig. 18. The pressure contour is influenced by both the curvature and nature of walls. In general, the pressure levels associated with the cavities having flexible sidewalls is higher than the cavities with rigid sidewalls. The influence of porosity distribution on pressure contour plots of the air-filled cavity having flexible porous walls is not much significant as seen in Fig. 19. However, there is a small variation in the pressure contour with respect to the nature of GPLs grading patterns as seen in Fig. 20.

8. Conclusions

Vibro-acoustic characteristics of fluid-filled cavity/tank with flexible sidewalls and curved top wall are analyzed using the higher-order finite element procedure. The effect of rigid and flexible sidewalls, thickness ratio, strong (water) and weak (air) fluid coupling, the curvature of top wall on the structural, fluid and coupled natural frequencies and sound pressure level of metallic and porous GPL reinforced composite tanks is detailed here. The influence of graded patterns of porosity and GPL are also investigated. Based on this comprehensive study, it is pronounced here as follows:

- The dynamic behavior of the acoustic cavity with rigid sidewalls is entirely different from the cavity with flexible sidewalls.
- The curvature angle of the top beam influences the coupled frequencies of the tank and SPL of the fluid cavity.
- Acoustic cavity having sidewalls made of porous GPLs with symmetric porosity and GPLs distribution enhances natural frequencies and sound pressure level.
- Variation in natural frequencies with an increase in wt.% of GPLs considered here is marginal.
- Pressure distribution inside the tank is significantly influenced by the curvature angle of the top wall and the vibrating nature of sidewalls.

- The difference between the structural and coupling frequency is high for the rigid sidewalls case whereas the frequency difference between fluid and coupled cases is more for the flexible sidewalls cavity.
- The SPL of the water-filled cavity is in general high compared to that of an air-filled cavity.

Data Availability

We have used the generic data available in the existing literature and the results are generated using our in-house code.

References

1. Gladwell G. M. L., Zimmermann G. On energy and complementary energy formulations of acoustic and structural vibrations problems. Journal of Sound and Vibration 1996;3(3): 233-241. https://doi.org/10.1016/0022-460X(66)90092-7
2. Gladwell G. M. L. A variational formulation of damped acousto-structural vibration problems. Journal of Sound and Vibration 1996;4(2):172-186. https://doi.org/10.1016/0022-460X(66)90120-9
3. Craggs. A. The transient response of a coupled plate-acoustic system using plate and acoustic finite elements. Journal of Sound and Vibration 1971;15(4):495-502. https://doi.org/10.1016/0022-460X(71)90408-1
4. Petyt M., Lea J., Koopmann G.H. A finite element method for determining the acoustic modes of irregular shaped cavities. Journal of Sound and Vibration 1976;45(4):495-502. https://doi.org/10.1016/0022-460X(76)90730-6
5. Wolf J. A. Modal synthesis for combined structural-acoustic systems. AIAA Journal 1977;15(5): 743-745. https://doi.org/10.2514/3.60685
6. Dowell E.H. Master plan for prediction of vehicle interior noise. AIAA Journal 1980;18(4):353-366. https://doi.org/10.2514/3.50767
7. Olson L. G., Bathe K. J. A study of displacement-based fluid finite elements for calculating frequencies of fluid and fluid-structure systems. Nuclear Engineering and Design 1983;76(2): 137-151. https://doi.org/10.1016/0029-5493(83)90130-9
8. Sandberg G., Göransson P. A symmetric finite element formulation for acoustic fluid-structure interaction analysis. Journal of Sound and Vibration 1988;123(3):507-515. https://doi.org/10.1016/S0022-460X(88)80166-4
9. Sandberg G. A new strategy for solving fluid-structure problems. International Journal for Numerical Methods in Engineering 1955;38(3):357-370. https://doi.org/10.1002/nme.1620380302
10. Alvelid M. Nonlinear fluid-structure interaction in propeller aircraft cabins. Journal of Vibration and Acoustics 1997;119(3): 363-373. https://doi.org/10.1115/1.2889732

11. Scarpa F., Curti G. A method for the parametric frequency sensitivity of interior acousto-structural coupled systems. Applied Acoustics 1999;58(4): 451-467. https://doi.org/10.1016/S0003-682X(99)00006-7
12. Ding P., Chen H. L. A symmetrical finite element model for structure acoustic coupling analysis of an elastic, thin-walled cavity. Journal of Sound and Vibration 2001;243(3):547-559. https://doi.org/10.1006/jsvi.2000.3478
13. Xiang Y., Huang Y. A semi-analytical and semi-numerical method for solving 2-D sound-structure interaction problems. Acta Mechanica Solida Sinica 2003;16(2):116-126. https://doi.org/10.1007/s1033830160116
14. Issac Harari. A survey of finite element methods for time-harmonic acoustics. Computer Methods in Applied Mechanics and Engineering 2006;195(13-16):1594-1607. https://doi.org/10.1016/j.cma.2005.05.030
15. Bermúdez A., Gamallo P., Hervella–Nieto L., Rodríguez R., Santamarina D. Fluid–Structure Acoustic Interaction, Computational Acoustics of Noise Propagation in Fluids - Finite and Boundary Element Methods. Springer, Berlin, Heidelberg. 2008. p.253-286. https://doi.org/10.1007/978-3-540-77448-8_10
16. Sandberg G., Wernberg P.A., Davidsson P. Fundamentals of Fluid-Structure Interaction. In: Computational Aspects of Structural Acoustics and Vibration. CISM International Centre for Mechanical Sciences, Springer, Vienna. 2008. p.505 23-101. DOI: 10.1007/978-3-211-89651-8
17. Jeong K.H. Hydroelastic vibration analysis of liquid-contained rectangular tanks. Structural Engineering and Mechanics 2011;40(5): 665-688. http://dx.doi.org/10.12989/sem.2011.40.5.665
18. Jeong K-H., Kim J-W. Free vibration analysis of liquid-filled open rectangular containers. Ocean Engineering 2015;99: 72-84. https://doi.org/10.1016/j.oceaneng.2015.03.003
19. Hernández E., Spa C., Caloenc S. A finite element approximations of a structural acoustic control problem with a Timoshenko beam interface. Journal of Mathematical Analysis and Applications 2015; 424(2):1125-1142. https://doi.org/10.1016/j.jmaa.2014.11.051
20. Hesse C., Perez J.M.V., Sinapius M. Frequency-independent radiation modes of interior sound radiation: An analytical study. Journal of Sound and Vibration 2017;392:31-40. https://doi.org/10.1016/j.jsv.2016.12.038
21. Dinachandra M., Sethuraman R. Isogeometric analysis for acoustic fluid-structure interaction problems. International Journal of Mechanical Sciences 2017; 131-132:8-25. https://doi.org/10.1016/j.ijmecsci.2017.06.041

22. Jhung M. J., Kang S-S. Fluid effect on the modal characteristics of a square tank. Nuclear Engineering and Technology 2019;51(4):1117-1131. https://doi.org/10.1016/j.net.2019.01.012

23. Bean M., Yi S-Y. A monolithic mixed finite element method for a fluid-structure interaction problem. Applied Mathematics and Computation 2019;363:124615. https://doi.org/10.1016/j.amc.2019.124615

24. Zhang H., Shi D., Zha S., Wang Q. Vibro-acoustic analysis of the thin laminated rectangular plate-cavity coupling system. Composite Structures 2018; 189:570-585. https://doi.org/10.1016/j.compstruct.2018.01.099

25. Hosseini S. A. H., Rahmani O. Free vibration of shallow and deep curved FG nanobeam nonlocal Timoshenko curved beam model. Applied Physics A: Materials Science and Processing 2016;169:122. https://doi.org/10.1007/s00339-016-9696-4

26. Akbaş Ş. D. Thermal effects on the vibration of functionally graded deep beams with porosity. International Journal of Applied Mechanics 2007;9(5):1750076. https://doi.org/10.1142/S1758825117500764

27. Ganapathi M., Polit O. Dynamic characteristics of curved nanobeams using nonlocal higher-order curved beam theory. Physica E: Low-dimensional Systems and Nanostructures 2017;91:190-202. https://doi.org/10.1016/j.physe.2017.04.012

28. Ebrahimi F., Daman M. Dynamic characteristics of curved inhomogeneous nonlocal porous beams in thermal environment. Structural Engineering and Mechanics 2017;64(1)121-133. http://dx.doi.org/10.12989/sem.2017.64.1.121

29. Ganapathi M., Merzouki T., Polit O. Vibration study of curved nanobeams based on nonlocal higher-order shear deformation theory using finite element approach. Composite Structures 2018;184: 821-838. https://doi.org/10.1016/j.compstruct.2017.10.066

30. Arefi M., E. Bidgoli M-Re, Dimitri R., Tornabene F., Reddy J. N. Size-dependent free vibrations of FG polymer composite curved nanobeams reinforced with graphene nanoplatelets resting on pasternak foundations. Applied Sciences 2019;9(8):1580.https://doi.org/10.3390/app9081580

31. Ganapathi M., Anirudh B., Anant C., Polit O. Dynamic characteristics of functionally graded graphene reinforced porous nanocomposite curved beams based on trigonometric shear deformation theory with thickness stretch effect. Mechanics of Advanced Materials and Structures 2019; 28(7): 741-752. https://doi.org/10.1080/15376494.2019.1601310

32. Anirudh B., Ganapathi M., Anant C., Polit O. A comprehensive analysis of porous graphene-reinforced curved beams by finite element approach using higher-order structural theory: Bending, vibration and buckling. Composite Structures 2019;222:110899. https://doi.org/10.1016/j.compstruct.2019.110899

33. Nicoletti R. On the natural frequencies of simply supported beams curved in mode shapes. Journal of Sound and Vibration 2020;485:115597. https://doi.org/10.1016/j.jsv.2020.115597

34. Chandra N., Raja S., Nagendra Gopal K.V. Vibro-acoustic response and sound transmission loss analysis of functionally graded plates. Journal of Sound and Vibration 2014;333(22): 5786-5802. https://doi.org/10.1016/j.jsv.2014.06.031

35. Affdl J., Kardos J. The Halpin–Tsai equation: A review. Polymer Engineering and Science 1976;16(5): 344–352. https://doi.org/10.1002/pen.760160512

36. Liu F., Ming P., Li J. Ab initio calculation of ideal strength and phonon instability of graphene under tension. Phys. Rev. B 2007;76(6): 064120. https://doi.org/10.1103/PhysRevB.76.064120

37. Shokrieh M., Esmkhani M., Shokrieh Z., Zhao Z. Stiffness prediction of graphene nanoplatelet/epoxy nanocomposites by a combined molecular dynamics–micromechanics method. Comput. Mater. Sci. 2014;92: 444–450. https://doi.org/10.1016/j.commatsci.2014.06.002.

38. Rafiee M. A., Rafiee J., Wang Z., Song H., Yu Z-Z, Koratkar N. Enhanced mechanical properties of nanocomposites at low graphene content. ACS Nano 2009;3(12):3884–3890. https://doi.org/10.1021/nn9010472

39. Villoria R. G. De , Miravete A. Mechanical model to evaluate the effect of the dispersion in nanocomposites. Acta Mater 2007; 55(9): 3025–3031. https://doi.org/10.1016/j.actamat.2007.01.007

40. Roberts A., Garboczi E. Elastic moduli of model random three-dimensional closed-cell cellular solids. Acta Mater 2001;49(2):189–197. https://doi.org/10.1016/S1359-6454(00)00314-1

41 Roberts A., Gaboczi E. Computation of linear elastic properties of random porous materials with a wide variety of microstructure. Proc. R. Soc. Lond. A. 2002;458(2021):1033–1054. https://doi.org/10.1098/rspa.2001.0900

42. Touratier M. An efficient standard plate theory. Internat. J. Engrg. Sci. 1991;29(8):901–916, http://dx.doi.org/10.1016/0020-7225(91)90165-Y.

43. Polit O, Merzouki T. Ganapathi M. Elastic stability of curved nanobeam based on higher-order shear deformation theory and nonlocal analysis by finite element approach. Finite Elem Anal Des. 2018;146:1–15. doi:https://doi.org/10.1016/j.finel.2018.04.002.

44. Polit O., Touratier M. A multilayered/sandwich triangular finite element applied to linear and non-linear analyses. Compos. Struct. 2002;58(1):121–128 https://doi.org/10.1016/S0263-8223(02)00033-8

List of Tables

List of Figures:

Fig. 9: Variation in sound pressure response for air cavity for various porosity distributions (e_p=*0.5*) for different curvatures with flexible boundaries at L/h=100. a) $\theta = 0°$; b) $\theta = 30°$

Fig. 10: Variation in sound pressure response for air cavity for various GPLs distributions (W_{gpl}=*1%*) for different curvatures with flexible boundaries at L/h=100. a) $\theta = 0°$; b) $\theta = 30°$

Fig 11: Variation in sound pressure response with different W_{gpl} and curvature angles for air cavity with rigid boundaries (e_p=*0.5*) i) L/h=30; ii) L/h=100.

Fig 12: Variation in sound pressure response with different W_{gpl} and curvature angles for air cavity with flexible boundaries (e_p =*0.5*) i) L/h=30; ii) L/h=100.

Fig. 13: Variation of sound pressure response with curvature angle for air cavity with W_{gpl}= *1%* with e_p =*0.5* for flexible boundaries. i)L/h=30; ii) L/h=100.

Fig. 14: Variation of sound pressure response with curvature angles for air cavity with W_{gpl}= *1%* with e_p =*0.5* for rigid boundaries. i)L/h=30; ii) L/h=100.

Fig. 15: Variation of sound pressure response for water cavity with curvature angles with W_{gpl}=*1%* , e_p =*0.5* for flexible boundaries. i)L/h=30; ii) L/h=100

Fig 16: Sound pressure response for curved beam (θ =30^0) with W_{gpl}=*0.5%* and e_p=0.5 for air cavity with two different type of boundary. a) L/h=30 b) L/h=100

Fig 17: Variation of sound pressure response in mediums for curved beam (θ =30^0) with W_{gpl}=*0.5% and* e_p=*0.5.*
a) L/h=30 b) L/h=100

Fig 18: Contour plots for air cavity with i) rigid walls and ii) flexible walls coupled with isotropic beam at respective frequencies (L/h=30) for various top beams. a) $\theta = 0°; b)\theta = 15°; c)\theta = 30°$

Fig: 19 Contour plots for air cavity with flexible boundary condition for various porosity distribution pattern (e_p=*0.5*) with *θ=30°* and L/h=100. a) Symmetric ; b) Unsymmetric ; c) Uniform porosity distribution.

Fig: 20 Contour plots for air cavity with flexible boundary condition for various GPLs distribution pattern *(W_{gpl}=1%)* with *θ=30°* and L/h=100. a) Symmetric ; b) Unsymmetric ; c) Uniform GPLs distribution.

Table1: Validation of natural frequencies (Hz) for air cavity with rigid boundaries and straight beam on top.

Mode No.	Present					Ref. [21]		
	Fluid Freq.	Structural Freq.		Coupled Freq.		Structural Freq.	Fluid Freq.	Coupled Freq.
		Classical	SSDT	Classical	SSDT			
1	17.000	12.831	12.815	13.145	13.130	12.836	17.000	13.153
2	34.000	51.265	51.017	16.953	16.952	51.346	34.000	16.953
3	42.500	115.122	113.89	34.036	34.036	115.528	42.500	34.037
5	51.000	317.824	308.85	44.806	44.770	320.915	51.000	44.815
10	85.004	1237.06	1122.8	67.978	67.977	1283.973	85.001	67.978

Table 2: Validation of natural frequencies (Hz) for air cavity with flexible boundaries and curved beam ($\theta = 30^0$) on top.

Mode No.	Structure Freq. (Hz)			Coupled Freq. (Hz)		
	Present	ANSYS	Error (%)	Present	ANSYS	Error (%)
1	14.8859	15.6563	4.920703	7.1234	7.8236	8.949844
2	23.57689	24.7083	4.579069	14.749	15.1844	2.867417
3	61.34079	62.9534	2.561593	20.431	20.3273	-0.51015
4	113.1536	114.155	0.877228	23.129	24.2181	4.49705
5	150.4364	150.882	0.29533	35.21	35.7449	1.496437
6	162.9578	162.043	-0.56454	40.299	39.3076	-2.52216
7	222.89178	224.886	0.886769	44.371	45.0418	1.489283
8	312.91127	313.270	0.114511	52.995	52.2583	-1.40973

Table 3: Effect of nature of sidewall on natural frequencies (Hz) of air cavity with straight beam on top.

Mode No.	L/h=30					L/h=100			
	Rigid			Flexible		Rigid		Flexible	
	Structural	Fluid	Coupled	Structural	Coupled	Structural	Coupled	Structural	Coupled
1.	13.8271	17.000	13.8752	17.5754	6.9920	4.1552	6.5568	5.3057	5.0340
2.	55.0010	34.000	16.9928	23.9127	17.5020	16.6125	14.2562	7.2421	5.2329
3.	122.6308	42.500	34.0077	67.6617	19.8214	37.3468	19.2199	20.6336	9.7007
4.	215.3292	45.774	42.5672	125.1763	23.8615	66.3170	32.7812	38.5255	18.5269
5.	331.3377	51.000	45.6619	163.0997	35.3512	103.4670	37.5841	50.5497	21.3490
6.	458.2575	54.426	50.9522	172.1276	43.8660	148.7271	43.4149	54.7788	35.0573
7.	468.6641	66.387	54.4297	241.7041	47.5583	202.0153	46.2614	77.0153	37.4829
8.	625.2145	68.001	55.1006	340.0683	52.5561	263.2396	50.8601	110.4628	44.3030
9.	798.9025	80.190	66.4243	381.4843	56.6397	332.2997	55.1755	139.8460	48.3509
10.	916.5151	85.004	67.9980	430.8473	67.1533	409.0896	63.1761	147.2351	49.0696

Table 4: Variation in structural and coupled frequencies (Hz) with distribution pattern of porosity (e_p=*0.5*) for air cavity with flexible boundaries and straight beam on top *(L/h=100)*

Mode No.	Symmetric		Unsymmetric		Uniform	
	Structural Freq.	Coupled Freq.	Structural Freq.	Coupled Freq.	Structural Freq.	Coupled Freq.
1.	5.2951	4.8541	4.8116	4.5341	4.7974	4.5252
2.	7.2272	5.2071	6.5653	4.7324	6.5483	4.7184
3.	20.5886	9.9583	18.6866	9.6762	18.6570	9.6698
4.	38.4354	18.3282	34.8562	17.1728	34.8353	17.1488
5.	50.4249	21.3993	45.8064	20.6939	45.7085	20.6879
6.	54.6164	34.9909	49.7202	33.7321	49.5332	33.7100
7.	76.7877	37.1894	69.8249	34.8516	69.6404	34.8403
8.	110.1110	44.4090	100.0217	44.2397	99.8860	44.2317
9.	139.3916	48.4971	126.6218	44.8679	126.4588	44.7771
10.	146.5419	48.7505	133.5274	48.4568	133.1441	48.4563

Table 5: Variation in structural and coupled frequencies with distribution pattern of GPLs (W_{gpl}=*1%*) for air cavity with flexible boundaries and straight beam on top *(L/h=100)*.

	Symmetric		Unsymmetric		Uniform	
Mode. No.	Structural Freq.	Coupled Freq.	Structural Freq.	Coupled Freq.	Structural Freq.	Coupled Freq.
1.	5.6859	5.2471	5.5598	5.1757	5.5396	5.1637
2.	7.7610	5.6063	7.5894	5.4821	7.5615	5.4623
3.	22.1114	9.9726	21.6171	9.8853	21.5435	9.8716
4.	41.2833	19.0306	40.3487	18.8917	40.2244	18.8675
5.	54.1663	22.2782	52.9582	21.9365	52.7789	21.8891
6.	58.6901	35.1550	57.4144	35.1269	57.1946	35.1216
7.	82.5153	40.0518	80.7055	39.1814	80.4117	39.0643
8.	118.3457	44.3833	115.7155	44.3581	115.3344	44.3549
9.	149.8238	48.3921	146.4772	48.3819	146.0139	48.3803
10.	157.6786	51.1127	154.2650	50.5963	153.7294	50.5014

Table 6: Natural frequencies (Hz) for air cavity with flexible walls with straight and curved beam on top with e_p =*0.5*, L/h=30.

		$\boldsymbol{\theta = 0°}$			$\boldsymbol{\theta = 15°}$			$\boldsymbol{\theta = 30°}$		
W_{gpl} *(%)*	Mode No.	Structural Freq.	Fluid Freq.	Coupled Freq.	Structural Freq,	Fluid Freq.	Coupled Freq.	Structural Freq.	Fluid Freq.	Coupled Freq.
	1.	17.8314	17.000	6.9893	17.1105	17.2634	7.0776	16.4697	17.4928	7.1755
	2.	24.2440	34.000	17.7320	25.4288	34.0874	17.0495	26.0498	34.0149	16.4274
	3.	68.5049	42.500	19.8469	68.3657	40.3235	20.0953	67.6021	38.5043	20.3403
	4.	126.5007	45.774	24.1778	125.5540	44.4972	25.3216	124.2509	43.2850	25.9055
0.25	5.	164.6166	51.000	35.3592	164.5385	51.1264	35.2660	164.8458	51.2708	34.9179
	6.	168.8582	54.426	43.8844	174.6402	53.1087	41.7188	176.8321	52.0439	40.0770
	7.	172.5921	66.387	47.5496	242.4422	65.1955	46.0489	241.4051	64.1448	44.6916
	8.	242.3294	68.001	52.5564	337.6810	68.0614	52.8093	335.1142	68.0850	53.0261
	9.	338.6908	80.190	56.6405	363.3239	79.0657	55.4284	366.4849	76.6100	54.4317
	10.	361.5236	85.004	67.5577	378.5392	80.6101	66.7133	425.7996	78.0326	65.7192
	1.	18.7381	17.000	6.9909	17.9807	17.2634	7.0789	17.307	17.4928	7.1766
	2.	25.4739	34.000	18.5687	26.7188	34.0874	17.8954	27.371	34.0149	17.2534
	3.	71.9647	42.500	19.9165	71.8185	40.3235	20.1192	71.016	38.5043	20.3517
	4.	132.8501	45.774	25.3912	131.8543	44.4972	26.5886	130.484	43.2850	27.1956
1	5.	172.8401	51.000	35.3643	172.7602	51.1264	35.2761	173.084	51.2708	34.9369
	6.	180.9973	54.426	43.8901	183.1627	53.1087	41.7260	185.478	52.0439	40.0839
	7.	254.1386	66.387	47.5602	254.2604	65.1955	46.0581	253.175	64.1448	44.7001
	8.	354.7458	68.001	52.5578	353.6898	68.0614	52.8107	351.007	68.0850	53.0276
	9.	375.6240	80.190	56.6419	377.4283	79.0657	55.4298	380.631	76.6100	54.4331
	10.	448.8696	85.004	68.1105	447.6508	80.6101	66.9928	445.381	78.0326	65.9712

Table 7 : Natural frequencies for water cavity with flexible walls with straight and curved beam on top with e_p =*0.5*, L/h=100

W_{gpl} (%)	Mode No.	$\theta = 0°$			$\theta = 15°$			$\theta = 30°$		
		Structural Freq.	Fluid Freq.	Coupled Freq.	Structural Freq.	Fluid Freq.	Coupled Freq.	Structural Freq.	Fluid Freq.	Coupled Freq.
	1.	5.3895	75.0000	2.7679	5.1709	76.1624	2.7034	4.9768	77.1744	1.0235
	2.	7.3560	150.000	4.4563	7.7159	150.385	4.3027	7.9047	150.065	2.6430
	3.	20.9554	187.501	5.8396	20.9119	177.897	5.8430	20.6794	169.872	4.2086
	4.	39.1197	201.945	9.0820	38.8388	196.311	9.1050	38.4448	190.963	5.8570
0.25	5.	51.3221	225.001	12.7407	51.2826	225.557	12.6898	51.3729	226.194	9.1964
	6.	55.5863	240.1188	19.7144	56.0941	234.3034	19.7709	56.6589	229.6056	12.7204
	7.	78.1516	292.8868	22.9609	78.1561	287.6272	23.1783	77.8039	282.9921	19.9683
	8.	112.0652	300.0063	28.4607	111.7393	300.2712	28.5726	110.9148	300.3751	23.6366
	9.	141.8651	353.7808	34.9805	141.7392	348.8193	35.1668	141.7154	337.9854	28.9872
	10.	149.1267	375.0193	44.3788	149.7429	355.6329	45.0476	150.9027	344.2615	35.6987
	1.	5.6648	75.0000	1.0218	5.4350	76.1624	1.0433	5.2310	77.1744	1.0705
	2.	77.7316	150.0002	2.8951	8.1099	150.3859	2.8276	8.3084	150.0658	2.7643
	3.	22.0251	187.5019	4.6593	21.9793	177.8979	4.4987	21.7350	169.8723	4.4003
	4.	41.1155	201.9455	6.1070	40.8202	196.3114	6.1105	40.4061	190.9632	6.1250
1	5.	53.9392	225.0015	9.5016	53.8977	225.5577	9.5259	53.9926	226.1947	9.6219
	6.	58.4152	240.1188	13.3262	58.9494	234.3034	13.2728	59.5433	229.6056	13.3047
	7.	82.1296	292.8868	20.6140	82.1345	287.6272	20.6733	81.7644	282.9921	20.8797
	8.	117.7654	300.0063	23.9945	117.4228	300.2712	24.2216	116.5561	300.3751	24.7004
	9.	149.0799	353.7808	29.7644	148.9475	348.8193	29.8820	148.9221	337.9854	30.3165
	10.	156.6655	375.0193	36.5901	157.3154	355.6329	36.7838	158.5369	344.2615	37.3386

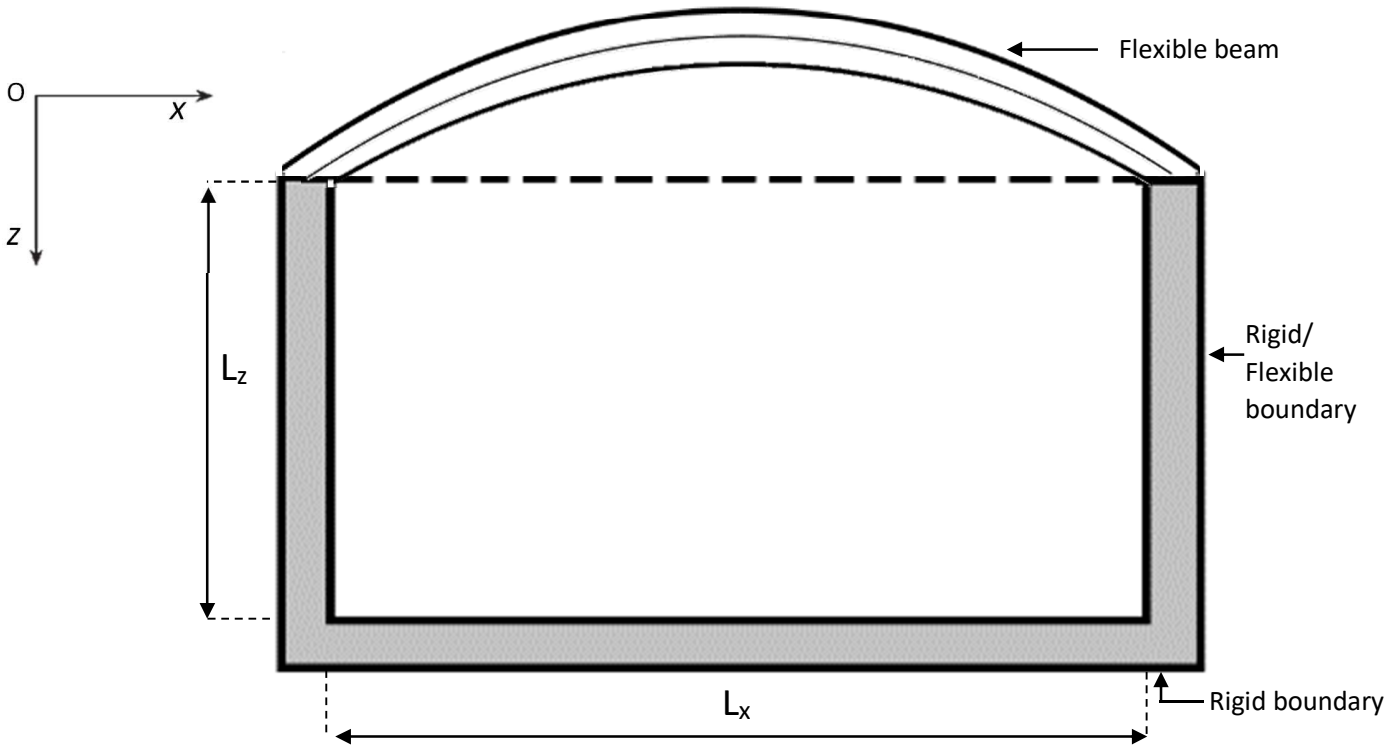

Fig. 1: Schematic representation of a curved beam simply supported on the acoustic cavity.

a) Porosity Distribution Type

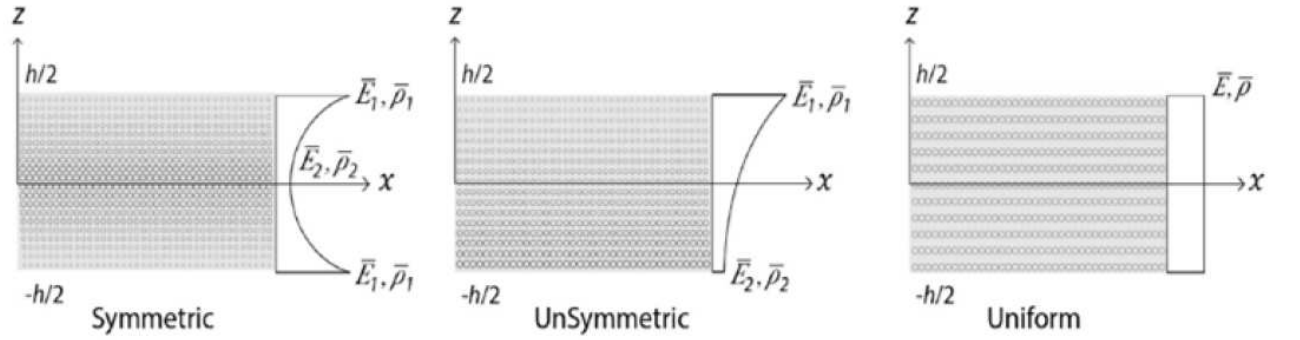

b) GPL Distribution Type

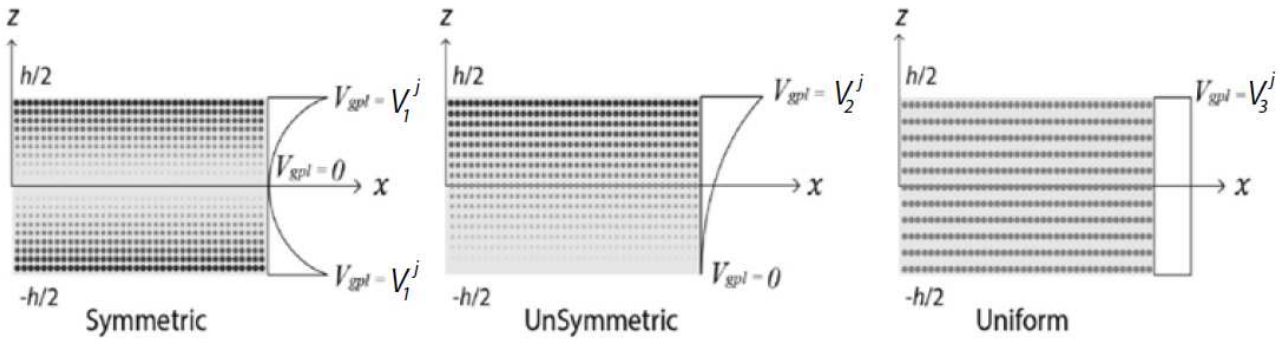

Fig. 2: Distribution pattern for porosity and GPLs through the thickness

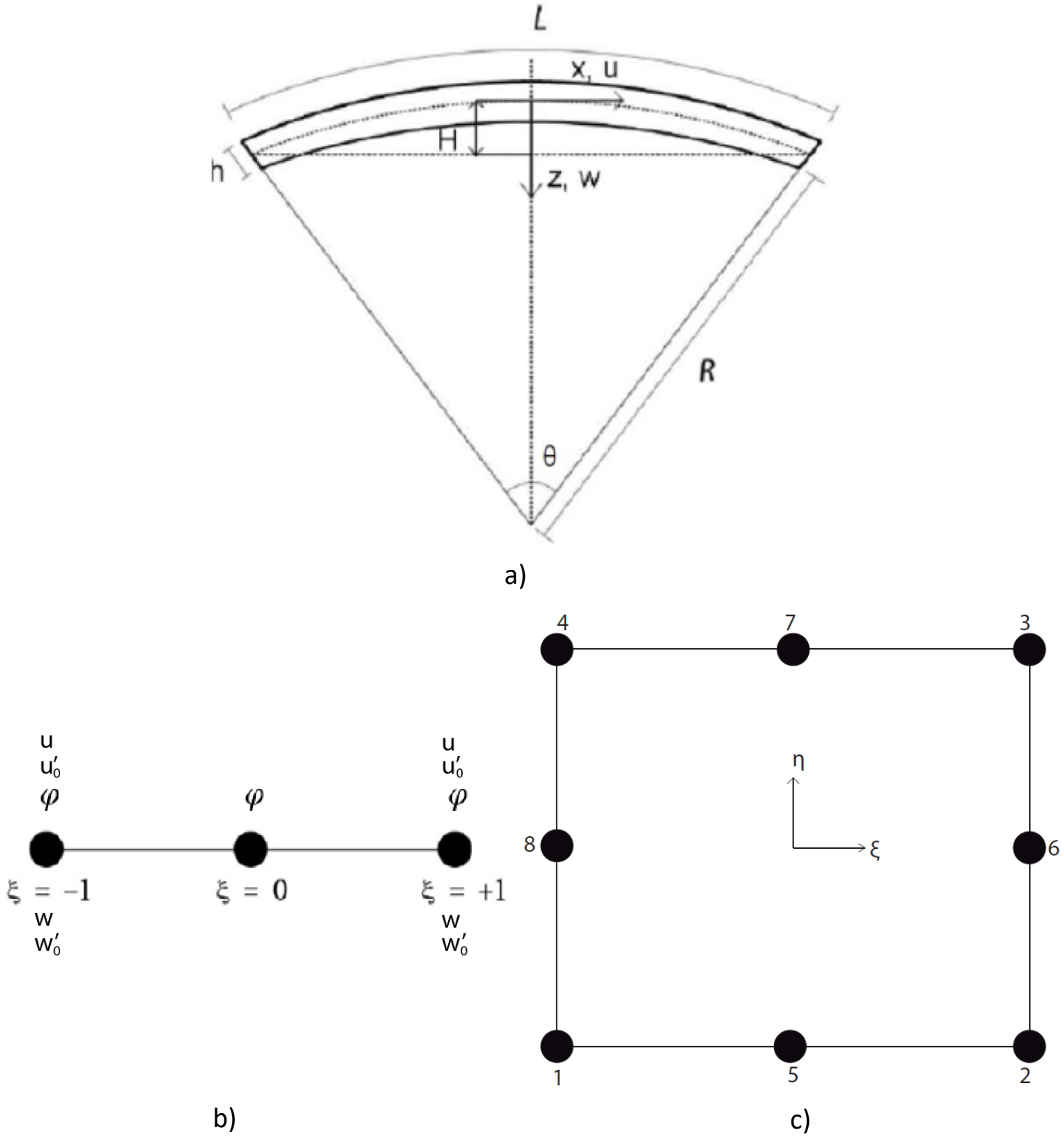

Fig. 3: a) Geometrical parameters of curved beam; b) Beam local element with the degrees of freedom; c) Isoparametric 8 noded fluid element.

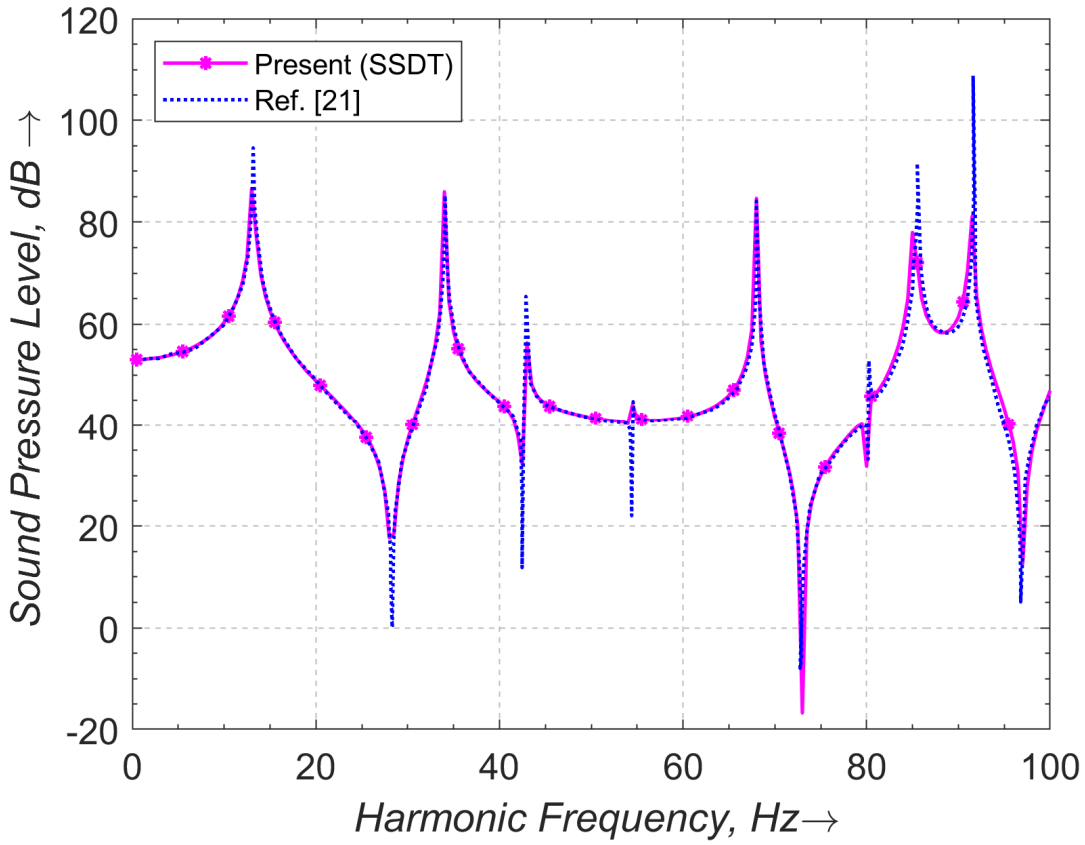

Fig 4: Comparison of variation of frequency vs SPL response for air cavity with rigid walls with Ref. [21] for straight beam on top.

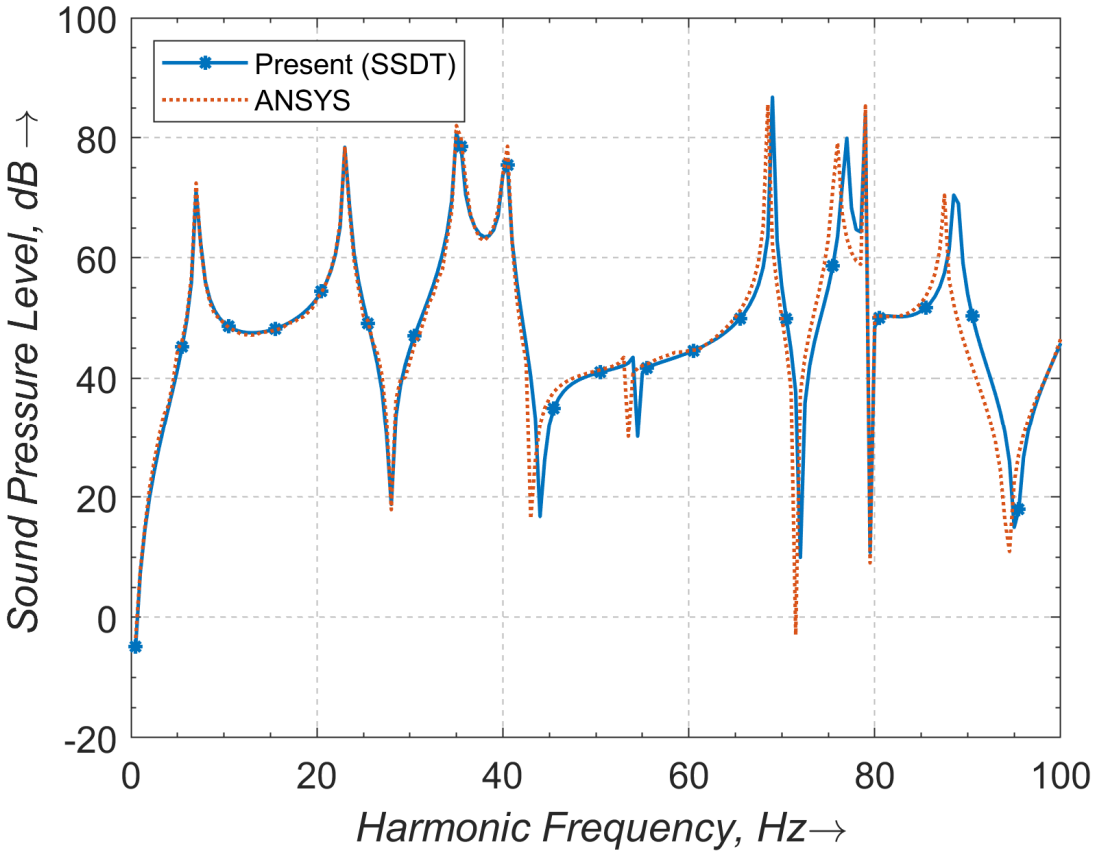

Fig.5 Comparison of present (SSDT) model with ANSYS for an isotropic air cavity with flexible walls and curved beam on top ($\theta = 30°$).

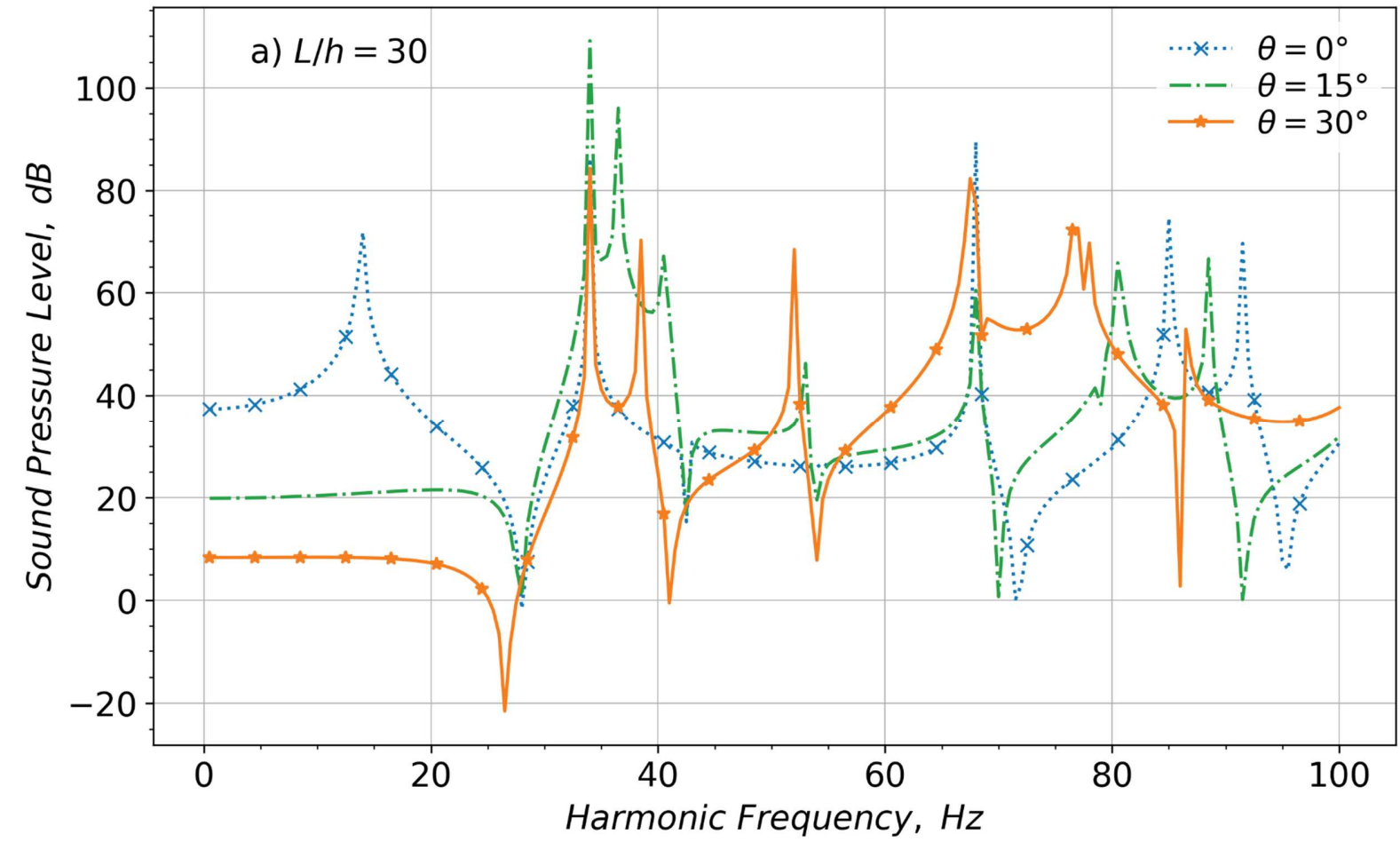

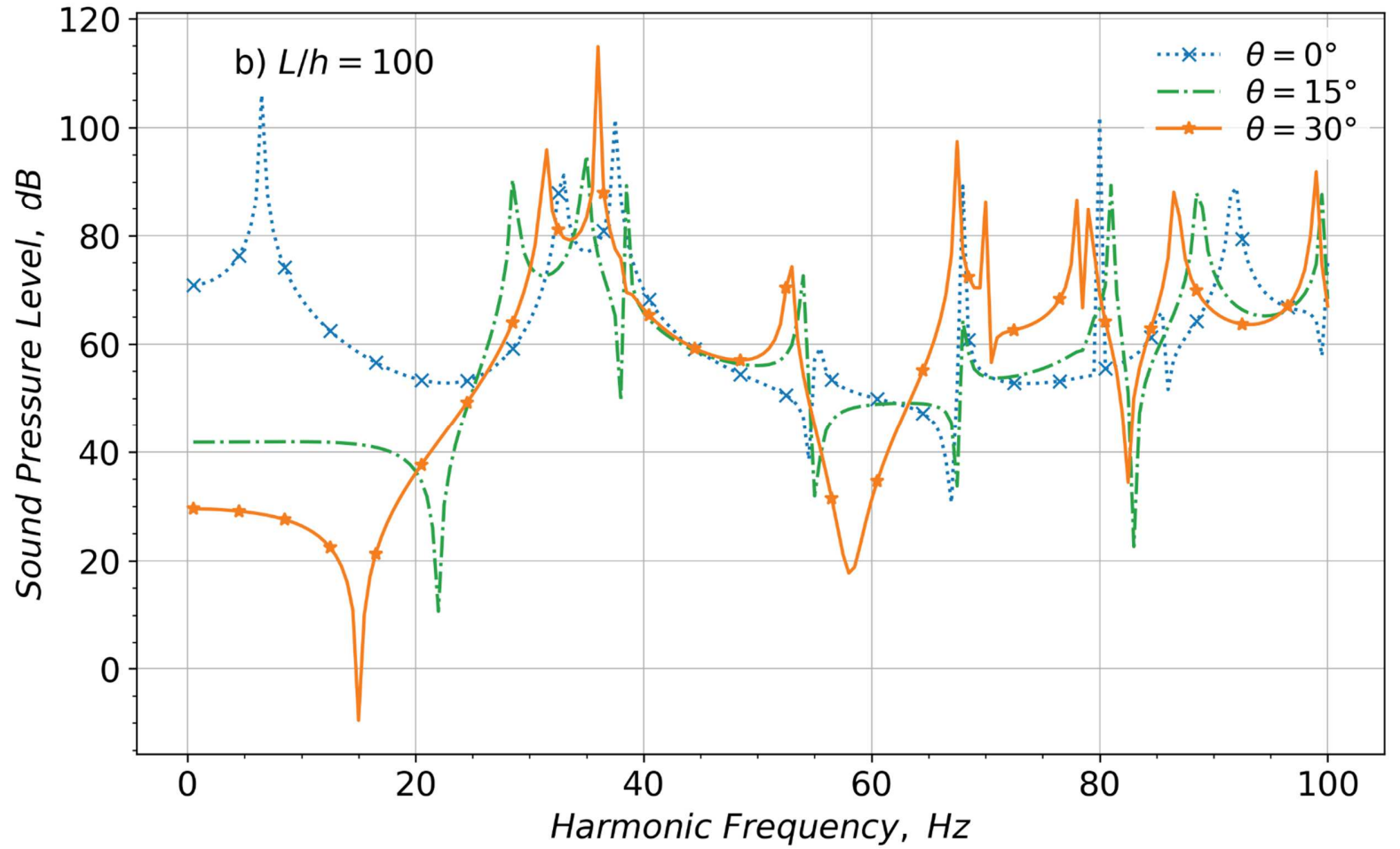

Fig 6: Influence of curvature angle on sound pressure response for isotropic air cavity with rigid walls: a) L/h=30; b) L/h=100.

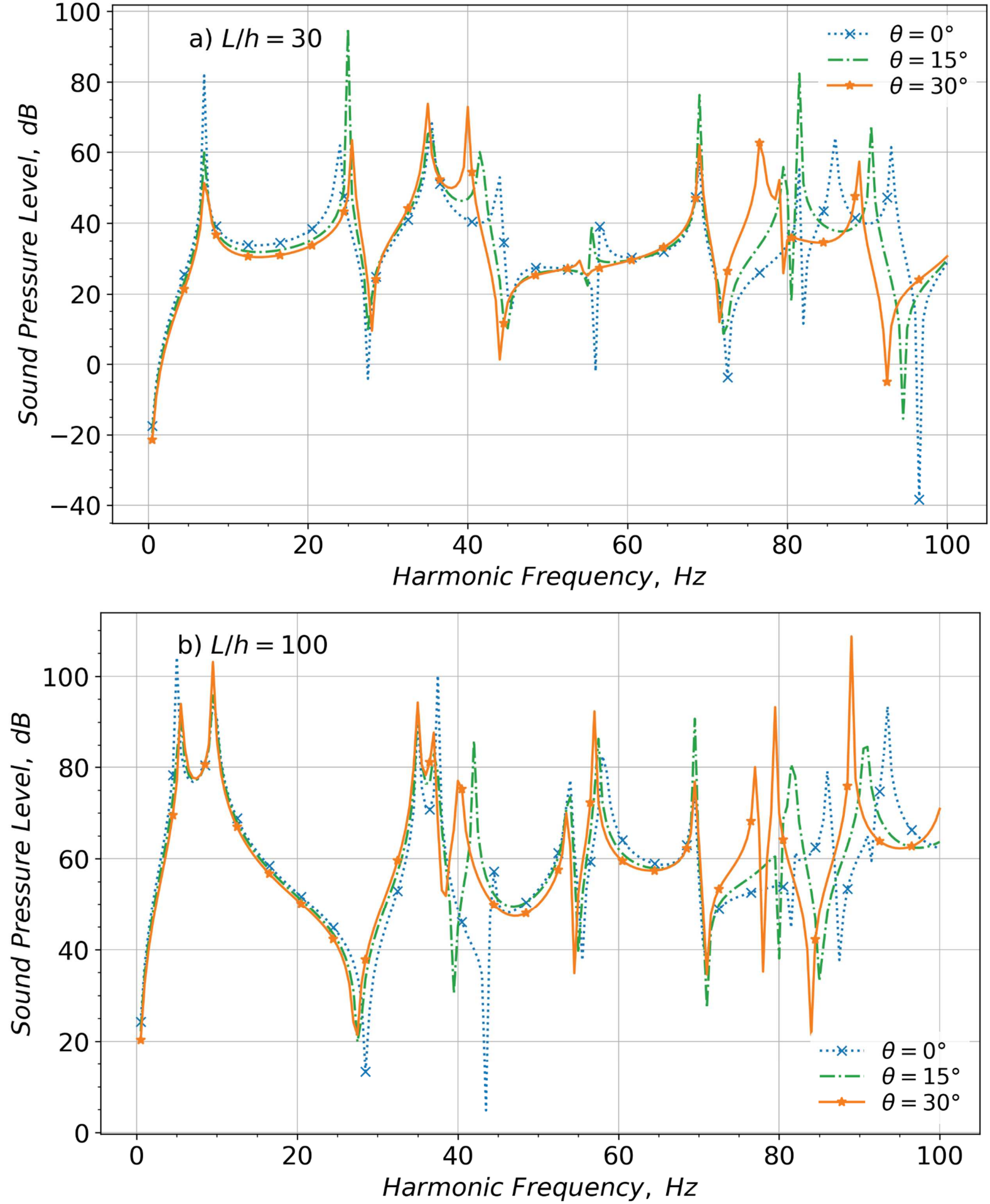

Fig 7: Influence of curvature angle on sound pressure response for isotropic air cavity with flexible walls a) L/h=30; b) L/h=100.

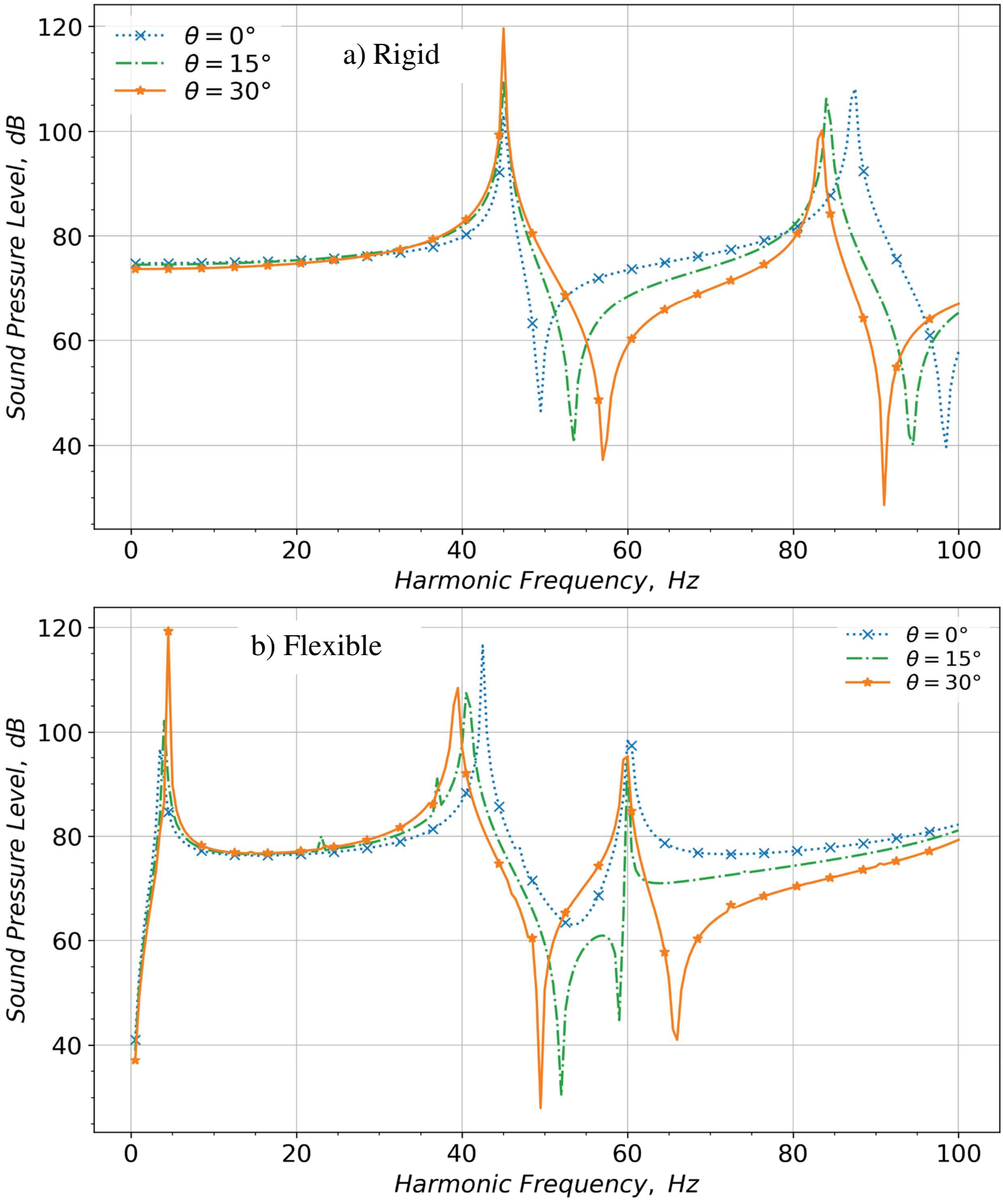

Fig. 8 Effect of different boundaries on sound pressure response for isotropic water cavity for L/h=30 with different curvatures. a) rigid and b) flexible boundaries.

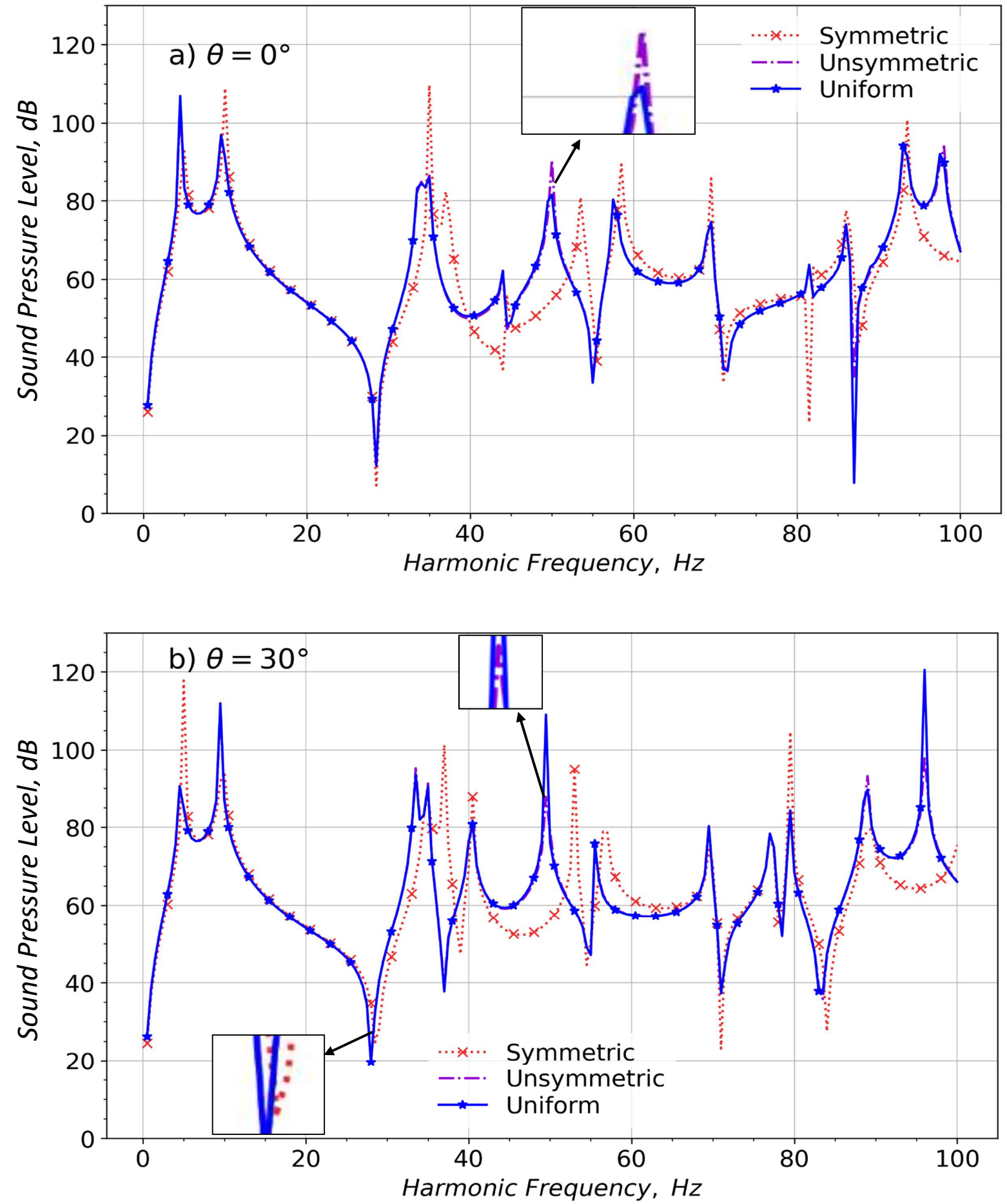

Fig. 9: Variation in sound pressure response for air cavity for various porosity distributions (e_p =*0.5*) for different curvatures with flexible boundaries at L/h=100. a) $\theta = 0°$; b) $\theta = 30°$

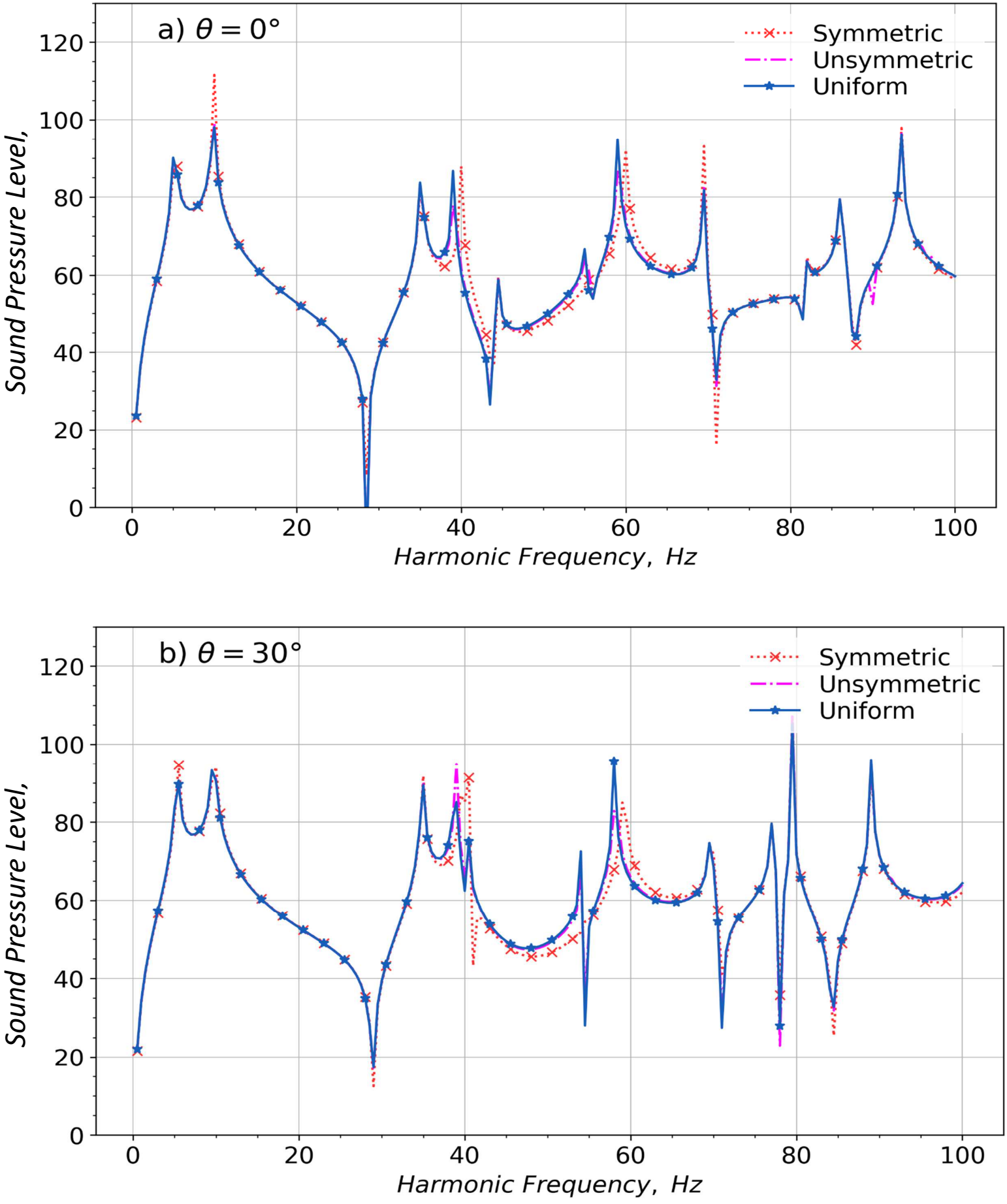

Fig. 10: Variation in sound pressure response for air cavity for various GPLs distributions (W_{gpl}=*1%*) for different curvatures with flexible boundaries at L/h=100. a) $\theta = 0°$; b) $\theta = 30°$

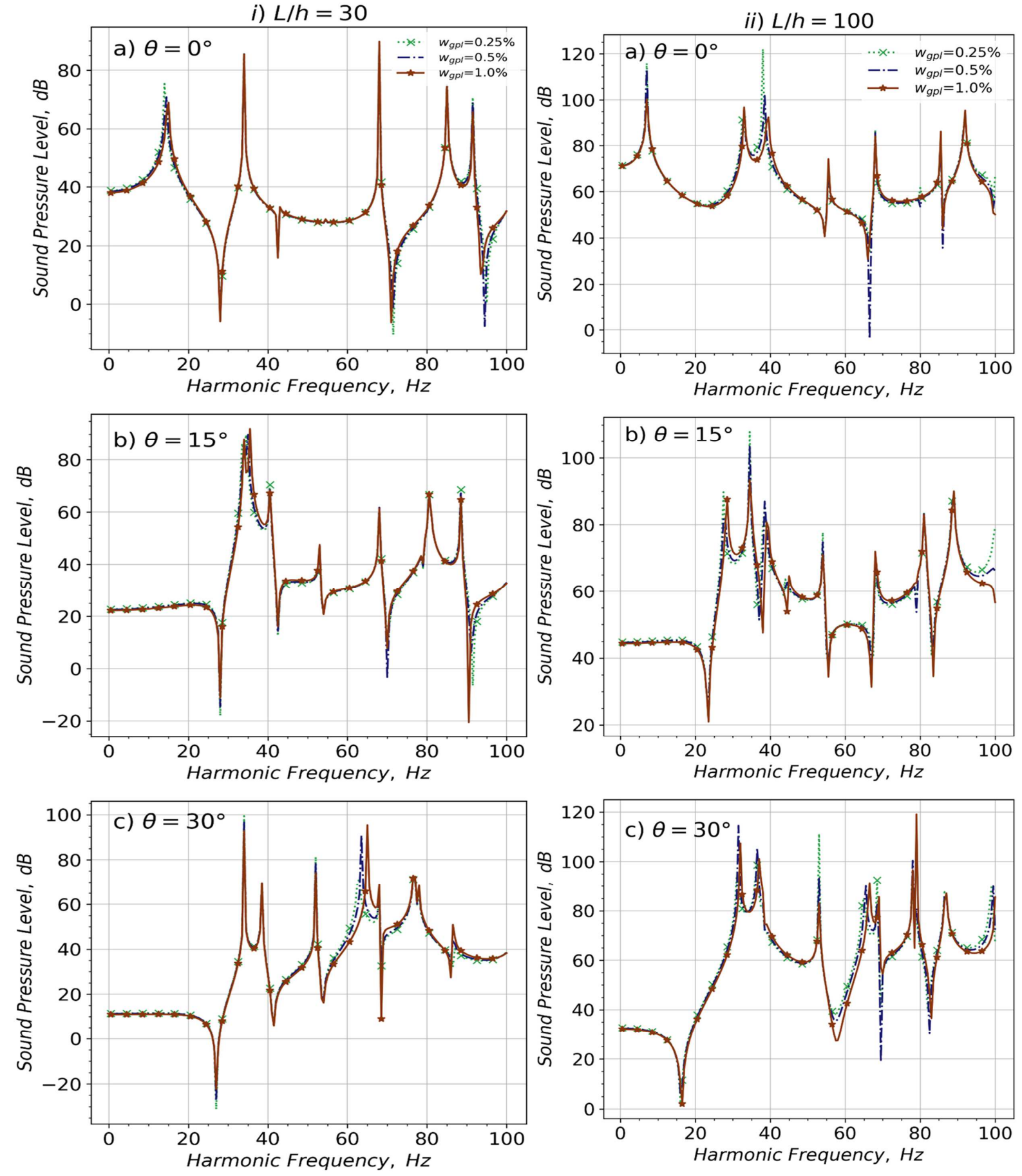

Fig 11: Variation in sound pressure response with different W_{gpl} and curvature angles for air cavity with rigid boundaries (e_p =0.5) i)L/h=30; ii) L/h=100.

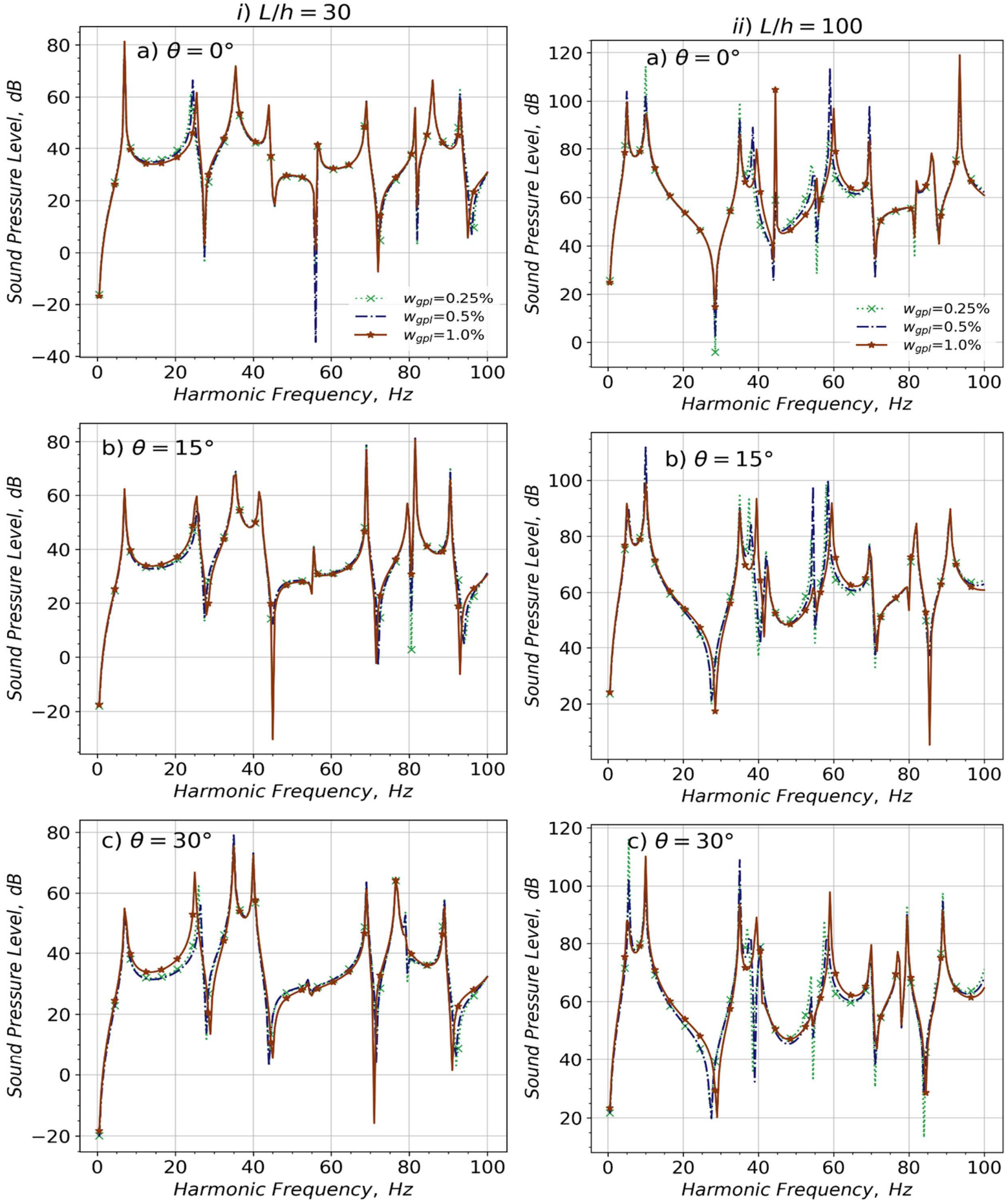

Fig 12: Variation in sound pressure response with different W_{gpl} and curvature angles for air cavity with flexible boundaries (e_p =0.5) i)L/h=30; ii) L/h=100.

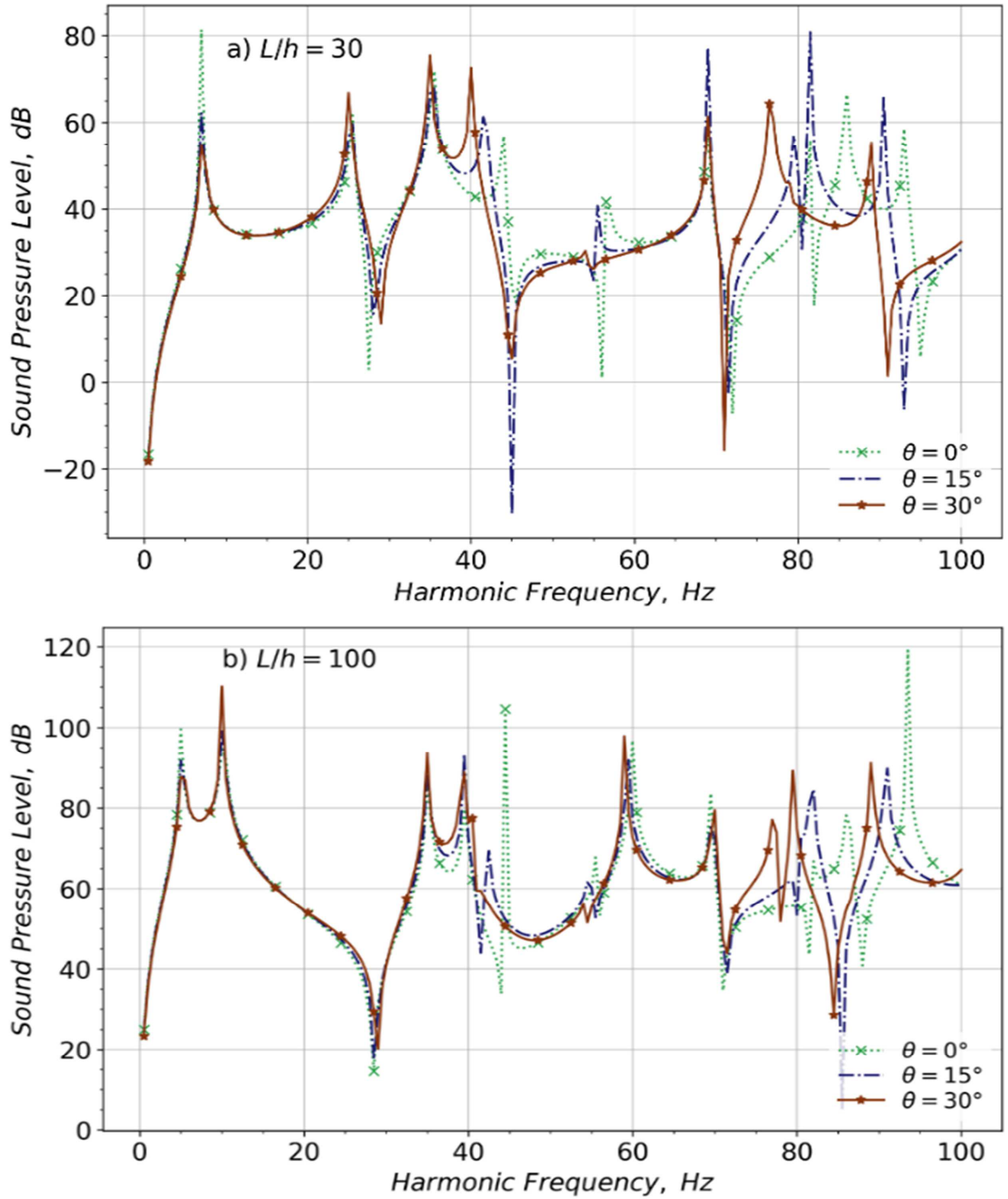

Fig. 13: Variation of sound pressure response with curvature angles for air cavity with W_{gpl}= *1%* and e_p =*0.5* for flexible boundaries. i)L/h=30; ii) L/h=100.

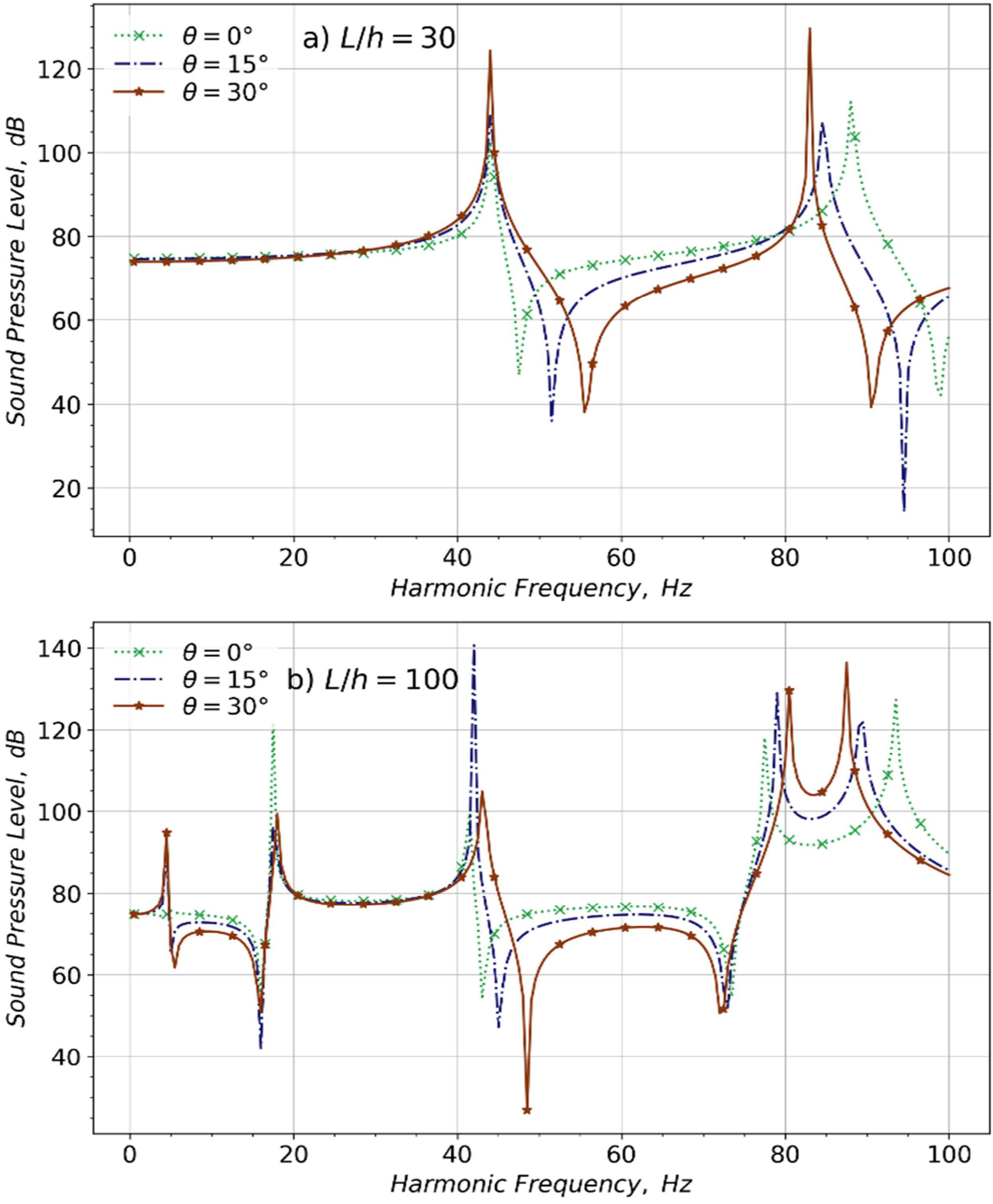

Fig. 14: Variation of sound pressure response with curvature angles for air cavity with W_{gpl}= *1%* and e_p =*0.5* for rigid boundaries. i)L/h=30; ii) L/h=100.

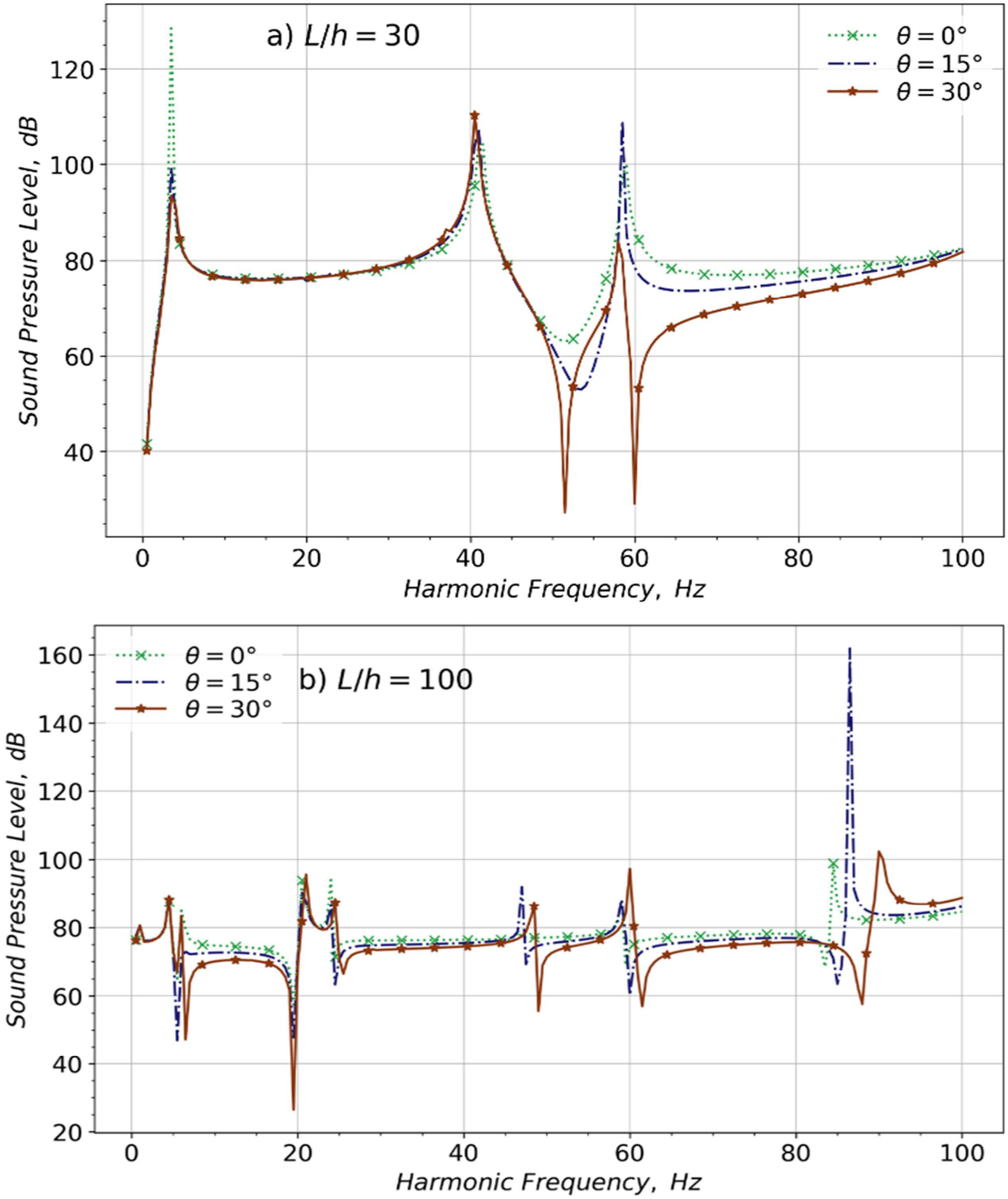

Fig. 15: Variation of sound pressure response for water cavity with curvature angles with W_{gpl}=*1%* and e_p =*0.5* for flexible boundaries. i)L/h=30; ii) L/h=100

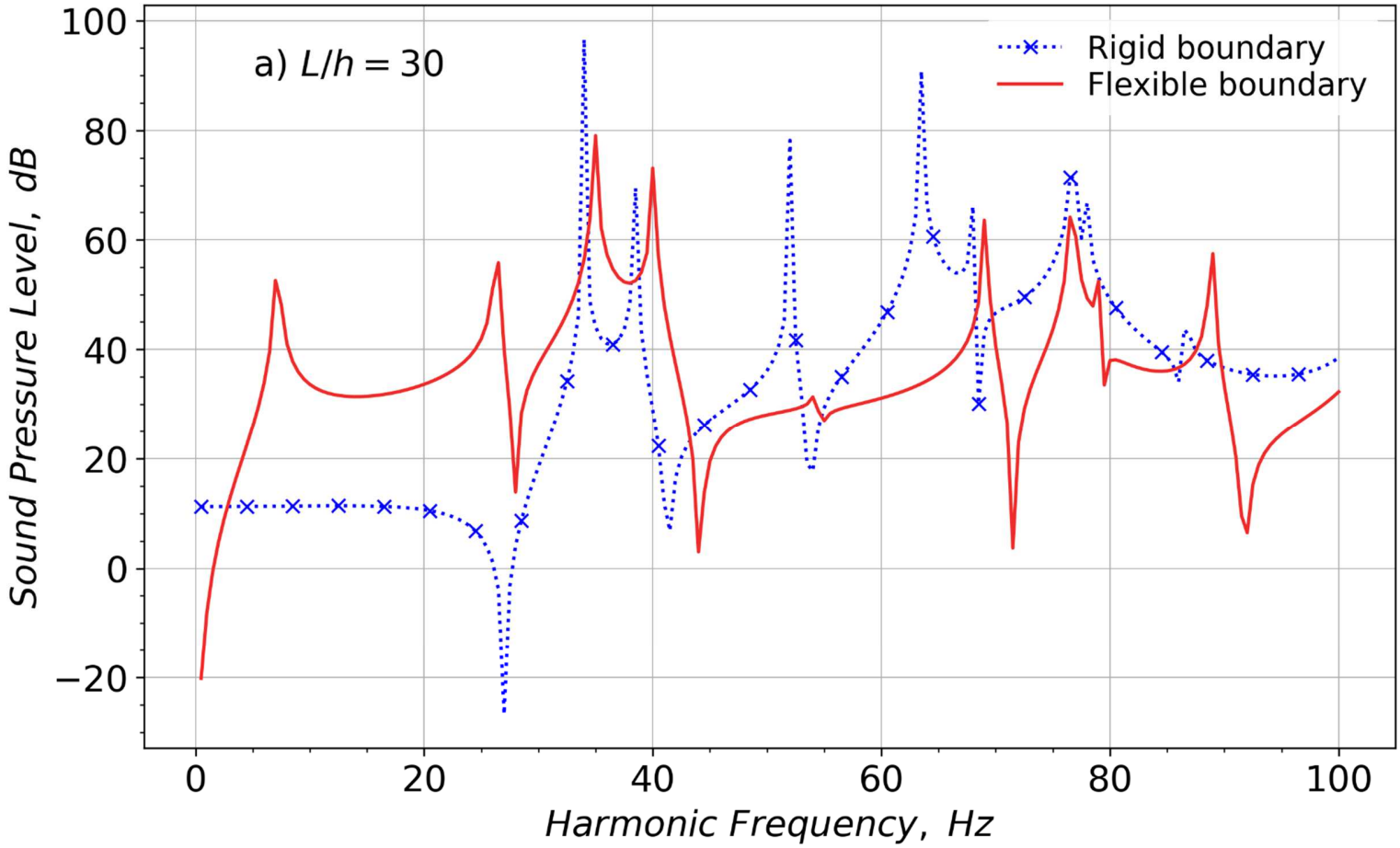

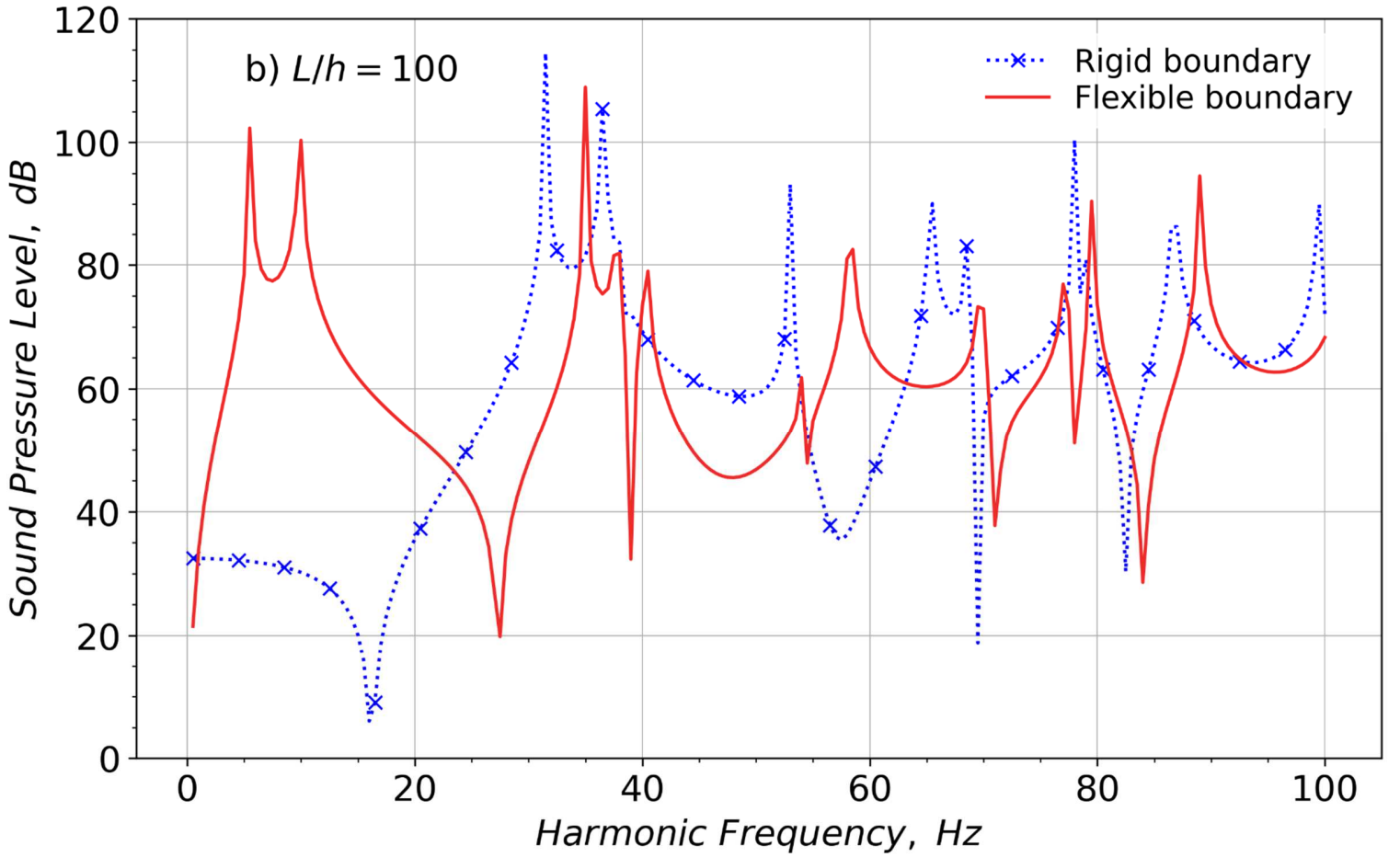

Fig 16: Sound pressure response for curved beam ($\theta = 30^0$) with W_{gpl}=0.5% and e_p =0.5 for air cavity with two different type of boundary. a) L/h=30 b) L/h=100

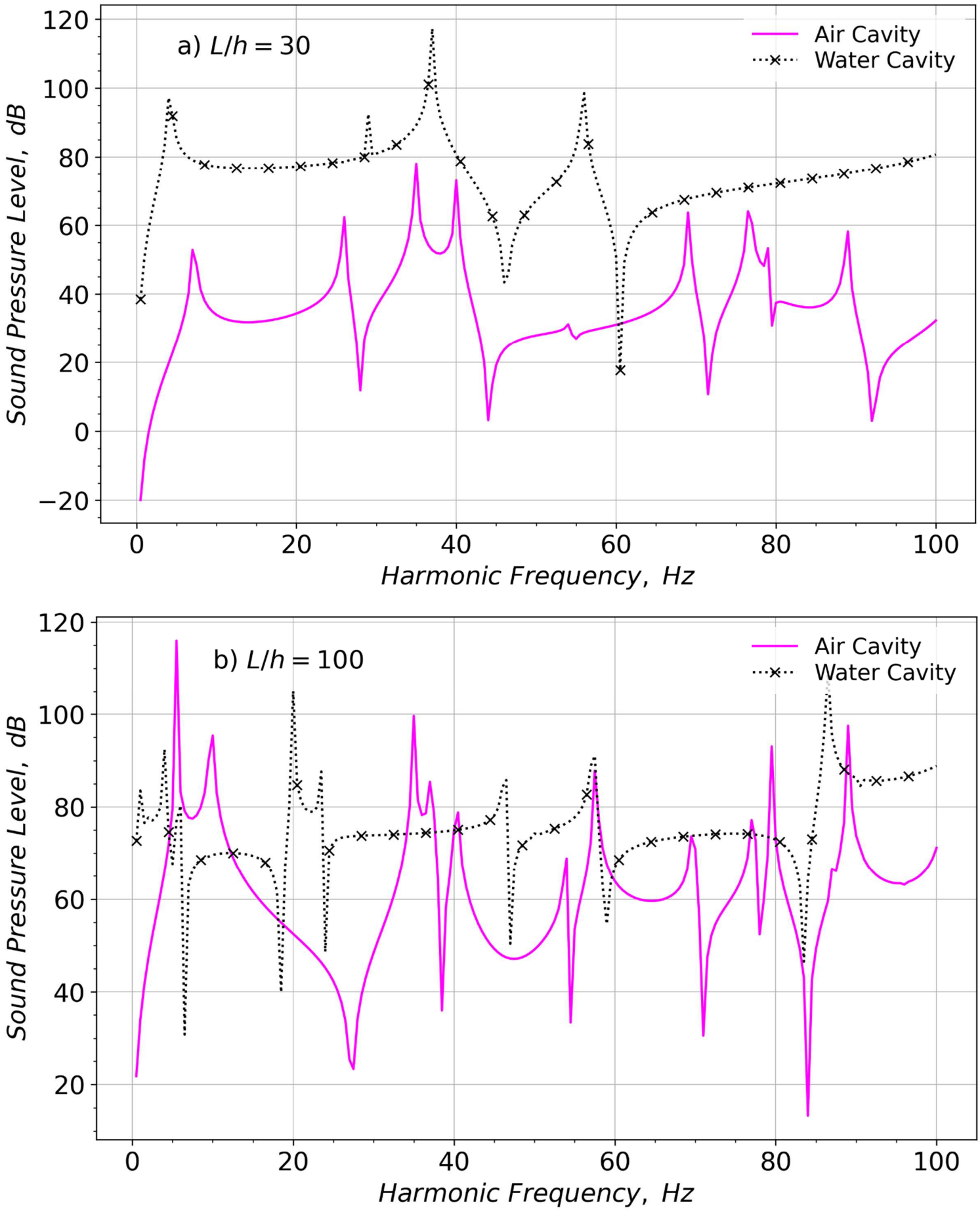

Fig 17: Variation of sound pressure response in different mediums for curved beam ($\theta = 30^0$) with W_{gpl}=0.5% *and* e_p =0.5. a) L/h=30 b) L/h=100 .

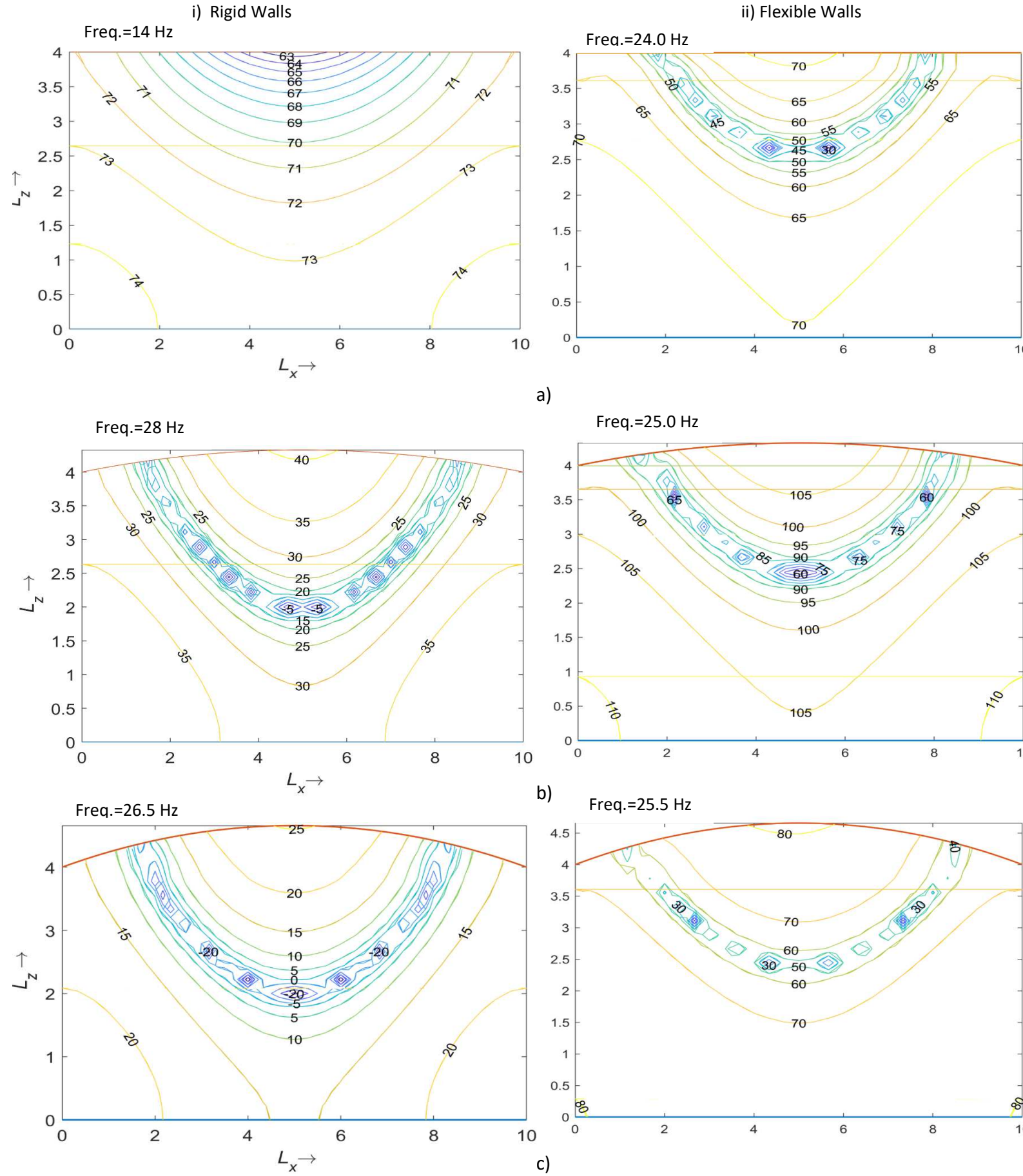

Fig 18: Contour plots for air cavity with i) rigid walls and ii) flexible walls coupled with isotropic beam at respective frequencies (L/h=30) for various top beams. a) $\theta = 0°; b)\theta = 15°; c)\theta = 30°$

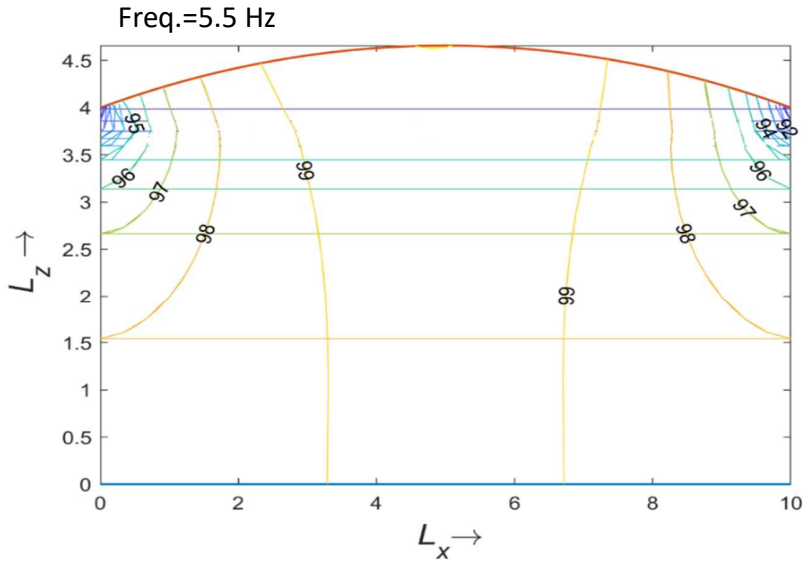

a)

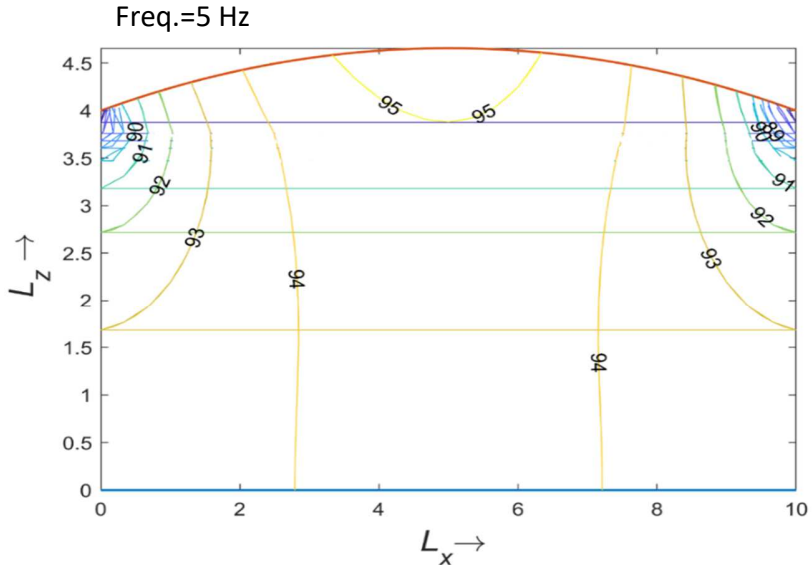

b)

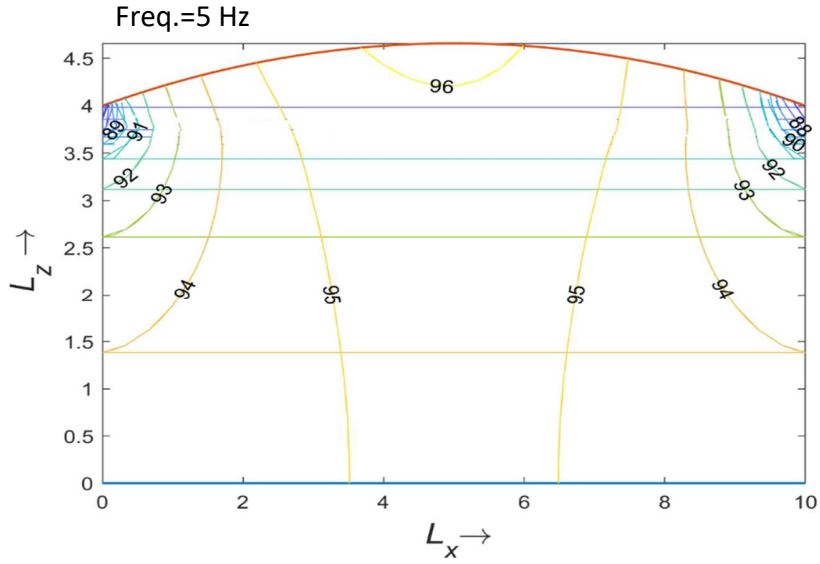

c)

Fig: 19 Contour plots for air cavity with flexible boundary condition for various porosity distribution pattern *(e_p =0.5)* with $\theta = 30°$ and L/h=100. a) Symmetric ; b) Unsymmetric ; c) Uniform porosity distribution.

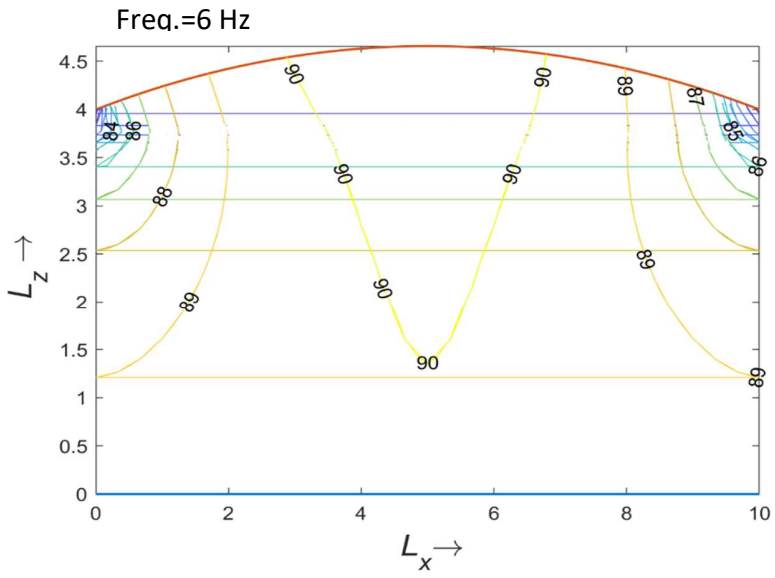

a)

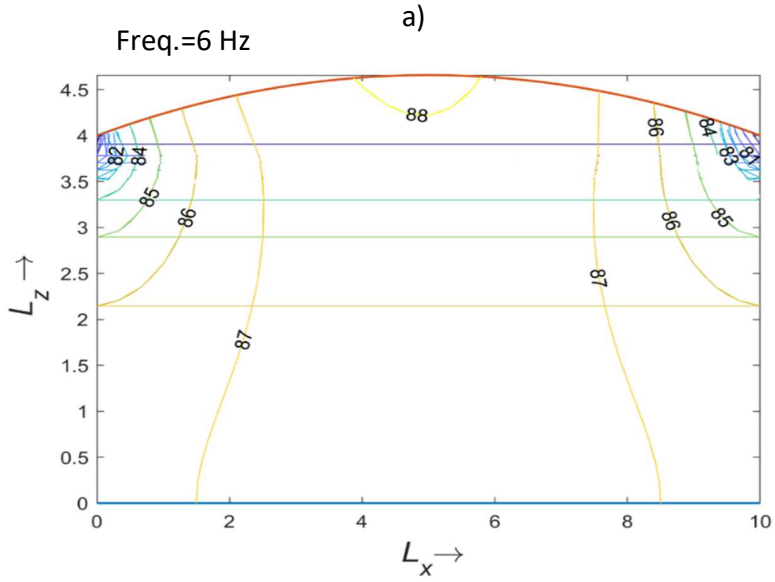

b)

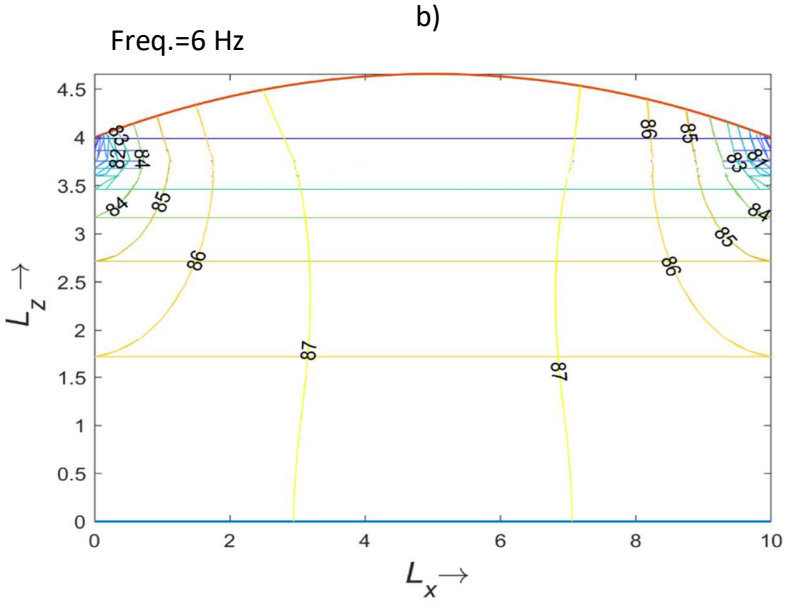

c)

Fig: 20 Contour plots for air cavity with flexible boundary condition for various GPLs distribution pattern *(W_{gpl}=1%)* with $\theta = 30°$ and L/h=100. a) Symmetric ; b) Unsymmetric ; c) Uniform GPLs distribution.